

C. Angioni, P. Mantica, T. Pütterich, M. Valisa, M. Baruzzo, E.A. Belli, P. Belo, F.J. Casson, C. Challis, P. Drewelow, C. Giroud, N. Hawkes, T.C. Hender, J. Hobirk, T. Koskela, L. Lauro Taroni, C.F. Maggi, J. Mlynar, T. Odstrcil, M.L. Reinke, M. Romanelli and JET EFDA contributors

Tungsten Transport in JET H-mode Plasmas in Hybrid Scenario, Experimental Observations and Modelling

“This document is intended for publication in the open literature. It is made available on the understanding that it may not be further circulated and extracts or references may not be published prior to publication of the original when applicable, or without the consent of the Publications Officer, EFDA, Culham Science Centre, Abingdon, Oxon, OX14 3DB, UK.”

“Enquiries about Copyright and reproduction should be addressed to the Publications Officer, EFDA, Culham Science Centre, Abingdon, Oxon, OX14 3DB, UK.”

The contents of this preprint and all other JET EFDA Preprints and Conference Papers are available to view online free at www.iop.org/Jet. This site has full search facilities and e-mail alert options. The diagrams contained within the PDFs on this site are hyperlinked from the year 1996 onwards.

Tungsten Transport in JET H-mode Plasmas in Hybrid Scenario, Experimental Observations and Modelling

C. Angioni¹, P. Mantica², T. Pütterich¹, M. Valisa³, M. Baruzzo³, E.A. Belli⁴, P. Belo⁵, F.J. Casson⁶, C. Challis⁶, P. Drewelow⁷, C. Giroud⁶, N. Hawkes⁶, T.C. Hender⁶, J. Hobirk¹, T. Koskela⁸, L. Lauro Taroni³, C.F. Maggi¹, J. Mlynar⁹, T. Odstreil¹, M.L. Reinke¹⁰, M. Romanelli⁶ and JET EFDA contributors*

JET-EFDA, Culham Science Centre, OX14 3DB, Abingdon, UK

¹*Max-Planck Institut für Plasmaphysik, Garching, Germany*

²*Istituto di Fisica del Plasma, CNR/ENEA, Milano, Italy*

³*Consorzio RFX-CNR/ENEA, I-35127 Padova, Italy*

⁴*General Atomics, PO Box 85608, San Diego, CA 92186-5608, USA*

⁵*Instituto de Plasma e Fusao Nuclear, IST, Lisbon, Portugal*

⁶*EURATOM-CCFE Fusion Association, Culham Science Centre, OX14 3DB, Abingdon, OXON, UK*

⁷*Max-Planck Institut für Plasmaphysik, Greifswald, Germany*

⁸*Aalto University, Association EURATOM-Tekes, P.O.Box 14100, FIN-00076 Aalto, Finland*

⁹*IPP.CR, Inst. of Plasma Physics AS CR, Prague, Czech Republic*

¹⁰*University of York, Department of Physics, Heslington, York, YO10 5DD U.K.*

* See annex of F. Romanelli et al, "Overview of JET Results", (24th IAEA Fusion Energy Conference, San Diego, USA (2012)).

ABSTRACT.

The behaviour of tungsten in the core of hybrid scenario plasmas in JET with the ITER-like wall is analyzed and modelled with a combination of neoclassical and gyrokinetic codes. In these discharges, good confinement conditions can be maintained only for the first 2 - 3 seconds of the high power phase. Later W accumulation is regularly observed, often accompanied by the onset of magnetohydrodynamical activity, in particular neoclassical tearing modes (NTMs), both of which have detrimental effects on the global energy confinement. The dynamics of the accumulation process is examined, taking into consideration the concurrent evolution of the background plasma profiles, and the possible onset of NTMs. Two time slices of a representative discharge, before and during the accumulation process, are analysed with two independent methods, in order to reconstruct the W density distribution over the poloidal cross-section. The same time slices are modelled, computing both neoclassical and turbulent transport components and consistently including the impact of centrifugal effects, which can be significant in these plasmas, and strongly enhance W neoclassical transport. The modelling closely reproduces the observations and identifies inward neoclassical convection due to the density peaking of the bulk plasma in the central region as the main cause of the accumulation. The analysis of a large set of discharges provides clear indications that this effect is generic in this scenario. The unfavorable impact of the onset of NTMs on the W behaviour, observed in several discharges, is suggested to be a consequence of a detrimental combination of the effects of neoclassical transport and of the appearance of an island.

1. Introduction

High-Z metallic materials, like Mo and W, can have good properties as plasma facing components (PFCs). In particular, W will be used in ITER and could be considered also in a future nuclear fusion reactor. The understanding of the behaviour of these highly radiating materials as PFCs, and the investigation of their impact on the plasma discharges is therefore of utmost importance. Recently JET has moved from a full carbon wall to the so-called ITER-like wall (ILW), which features W as the plasma facing material in the divertor, and Be in the main chamber walls [1, 2]. The consequences of the change of the PFCs on the achievability of plasma scenarios and on the performance are a topic of extreme interest, and have been considered in several recent studies [3–5]. In the framework of this research, a particularly important element is the experimental characterization and theoretical understanding and modelling of the W behaviour in the plasma core, where central accumulation can take place and can prevent the regular development of a plasma scenario. Recent attempts to re-establish the hybrid scenario [6–8] in JET with the ILW (JET-ILW) were successful [3], but, at the same time, they have been confronted with the difficulty that this scenario, developed with neutral beam injection (NBI) heating only, is particularly prone to W accumulation. This limits the duration of the high power phase with good confinement.

This realization has given priority to the study of the dynamics of the W behaviour in the core of JET–ILW hybrid scenario plasmas, by means of the combination of a detailed analysis of the experimental observations, and dedicated modelling with theoretical models describing both neoclassical and turbulent transport. The present research therefore aims at contributing to the general understanding of the transport of heavy impurities in the core of tokamaks, a topic which has received particular consideration over the last decade, from both the experimental [9–20] and the theoretical [21–30] standpoints.

The specific goal of the study presented in this paper is to identify the dominant mechanisms responsible for W accumulation in the JET–ILW hybrid scenario. To this end, analysis of the time evolution of W behaviour in these discharges is performed in combination with theory-modelling of the W density at representative time slices.

Two complementary diagnostic methods have been used to reconstruct the two dimensional (2D) W density over the poloidal cross section. The first is based on interpretive transport simulations of the W and Be density profiles, assumed as the two main impurities in these plasmas, with the 1D JETTO/SANCO transport code [32], in combination with the UTC [33] and the SXRPY [34] post-processor codes.

The second method is based on a direct soft X-ray (SXR) W density interpretive diagnostic [5,31]. With this technique, the bremsstrahlung emission of low Z ion species is subtracted from the total SXR emission and the 2D W density distribution is obtained by best fitting the residual SXR emission with a model-based deconvolution.

By this two-pronged diagnostic approach, not only the direct comparison with the theoretically predicted 2D W density becomes possible, but also between two independent diagnostic techniques, which also allows us to estimate the uncertainty in the determination of the absolute W density. In addition, comparisons with results of the tomographic reconstructions of the SXR emission are shown. In this case no assumption is made on the 2D W density functional form, and in particular on the dependence on the poloidal angle. Therefore this can be considered an additional complementary validation test for the theoretical predictions.

These comparisons provide an example of the present theoretical capabilities in predicting the transport of W in the core of high confinement tokamak plasmas.

In the framework of the theory-based modelling carried out in this work, the neoclassical and turbulent transport calculations have been performed with the drift-kinetic (DK) code NEO [35,36] and the gyrokinetic (GK) code GKW [37,38] respectively. These codes are used since they include the consistent treatment of centrifugal effects on transport, and in particular the impact of the poloidal asymmetry of the W density. The inclusion of these effects is necessary to model W in these plasmas, where the central thermal Mach number of D can be as high as 0.4, and therefore the central ratio of toroidal velocity to W thermal velocity v_ϕ/v_{thW} is above 3.8. The modelling is shown to closely reproduce the W transport behaviour observed in the experiment, and indicates that neoclassical convection due to the density peaking of the bulk plasma in the center is the cause of the observed accumulation. This result has motivated a more general characterization of the experimental behaviour of W in this scenario, in order to assess the general validity of the conclusions drawn from the modelling of only two time-slices of a single discharge.

The paper is organized as follows. In Section 2, the discharge scenario and the dynamics of the experimental behaviour of W are briefly described. Section 3 introduces the approach applied in the modelling, and compares the relative contributions of neoclassical and turbulent transport. In Section 4, the results from both the diagnostic techniques and the comparison with the theoretical predictions are presented. Subsection 4.1 describes the analysis based on the JETTO/SANCO interpretive modelling, and Subsection 4.2 describes the SXR 2D W density diagnostic. In Subsection 4.3 both the experimentally reconstructed W densities, as well as the tomographic inversions of the SXR emission, are compared with the theoretical predictions of two time slices of a representative JET–ILW hybrid scenario discharge, one time slice before the start of W accumulation, and one during W accumulation. In Section 6, the generality of the conclusions drawn from the theory–based modelling of a single discharge is investigated. Moreover, the impact of magneto-hydrodynamic (MHD) activity on the W behaviour is also considered. In particular, the potential interplay between radial transport and the onset of neoclassical tearing modes (NTMs), which in some cases are observed to impact the W behaviour, is examined. Finally, in Section 7 the main conclusions are presented and the implications for future research are outlined.

2. W behaviour in JET–ILW hybrid scenarios

The time traces of a representative JET–ILW discharge in hybrid scenario (shot #82722, $B_T = 2$ T, $I_p = 1.7$ MA, low triangularity) are presented in Fig. 1. This discharge displays a rather stable behaviour, reaching relatively good performance early in the high heating power phase, but with performance degradation at later times (b). Although the total radiated power in this discharge remains constant (a), we observe a progressive increase of the signal of the most central line of sight of the vertical camera (t_{19} in (e)) with respect to a more peripheral line of sight (t_{25} in (e)) on the low field side (LFS) of the JET SXR diagnostic system [39]. As will be clarified later, this is produced by a progressive accumulation of W in the region close to the magnetic axis. Early in the high power phase, the central density is lower than the density around mid-radius, which is the signature of a locally hollow density profile (d). Later, the central density peaks, while two big sawtooth crashes limit the increase of central density peaking (d), as well as the increase of central SXR emission (t_{19} in (e)). This transient behaviour of the electron density is of interest in this context, as will be demonstrated in the following sections, and is better illustrated in Fig. 2, where the density and temperature profiles, as measured by the high resolution Thomson scattering (HRTS) system, are plotted for selected times during the high power phase. After the NBI heating power is switched on (full power reached at 4.8s) and the plasma goes into H–mode (at 4.82s, with first ELM at 5.13s), the edge electron density increases quickly and forms the edge pedestal, but this increase at the edge is not directly followed in the central density. The density profile develops a negative radial gradient (that is, a peaking) in the region outside $r/a = 0.4$ in the first few hundred milliseconds, but takes much longer to develop a peaking in the centre of the plasma, where the density profile remains hollow (with

positive radial gradients) for at least 1 s. This behaviour, which is regularly observed in the JET–ILW hybrid scenario in response to the switch on of the NBI and the access into H–mode, appears to be generic in a large device like JET. It has been recently observed and analysed also in high density H–modes in standard scenario, where the phase of centrally hollow density profile can last several seconds [40]. In Fig. 2 the profiles plotted in bold correspond to the time slices at 5.9 s and 7.5 s which have been selected for the specific analysis, presented in the next two sections. The corresponding profiles of the ion temperature and of the toroidal rotation at these two time slices are presented in Fig.3. As will be clear from the results presented in Section 3, the detailed study and comparison of these two time slices is of interest because the first, at 5.9 s, is before the start of the W accumulation process, whereas the second, at 7.5 s, is during a phase of W accumulation. This can be realized from Fig. 11(e). At 5.9 s the t_{19} signal (SXR central line of sight (LOS)) is below the t_{25} signal (SXR LFS off–axis signal), whereas at 7.5 s t_{19} largely exceeds t_{25} . Tomographic inversions of the SXR emission, as well as W densities reconstructed from the interpretive modelling with the JETTO/SANCO package and from the 2D SXR W density diagnostic at these two time slices will be presented in Section 4. These results will be directly compared with those obtained from the theoretical modelling of the W transport for the same time slices. Before showing the results of this comparison, the theory–based modelling approach is described in the next section.

3. Theoretical modelling of W transport

The two time slices 5.9 s and 7.5 s have been considered for the computation of W transport with theoretical models. The DK code NEO [35, 36] has been utilized to compute the neoclassical transport component, whereas the GK code GWK [37, 38] has been applied to compute the turbulent transport. The linear GK calculations have been performed over a spectrum from $k_y \rho_i = 0.15$ to $k_y \rho_i = 0.7$, where k_y is the binormal wave number and $\rho_i = \sqrt{T_i/m_i}/\Omega_{ci}$. Quasi–linear transport has been computed assuming a peak of the non–linear spectrum around $k_y \rho_i = 0.25$, which is found to be appropriate for quasi–linear impurity transport calculations in ion temperature gradient (ITG) turbulence [48]. The calculations include the realistic plasma geometry as computed by polarimetry constrained EFIT equilibrium reconstructions [49–51]. We stress that the two time slices have been selected since they are representative of two conditions during the time evolution of the high power phase of the discharge. In the calculations, a single W species is considered, with a charge which changes along the minor radius and is given by the local average over the concentrations of all the W ionization stages, which, in the ranges of electron temperature of these plasmas, varies from $Z_W \simeq 45$ in the center to $Z_W \simeq 35$ at the boundary of the simulation domain ($r/a = 0.85$). Turbulent transport calculations do not include other impurity species, but include the actual value of the effective charge number Z_{eff} in the collision frequency. The W concentration in the experiment is found to be of the order of 10^{-4} , which implies that W behaves as a trace in these calculations. In contrast to the turbulent transport calculations, the neoclassical calculations include Be as additional impurity species, in order to also take

into account the effect of collisions between W and Be. Also NEO calculations take into account the realistic magnetic equilibrium geometry from EFIT. Due to the high value of v_ϕ/v_{thW} , centrifugal effects produce a poloidal asymmetry of the W density distribution [52,53]. Therefore, the W density as well as the W density gradient become functions of the poloidal angle θ and a reference position has to be defined in order to express the W particle flux. In both NEO and GKW calculations the reference position which has been considered is the LFS, that is the $\theta = 0$ position. The flux surface averaged W radial particle flux Γ_W is given by

$$\frac{R\Gamma_W}{n_W} = -(D_{WNEO} + D_{WGKW})\frac{R}{L_{nW}} + (RV_{WNEO} + RV_{WGKW}),$$

where the normalized logarithmic density gradient R/L_{nW} is computed considering the LFS radial density gradient and the LFS density. The time evolution of the flux surface averaged W density is governed by a continuity equation, which, assuming that the magnetic equilibrium geometry is not evolving in time, reads

$$\frac{\partial n_W}{\partial t} + \frac{1}{V'}\frac{\partial}{\partial \rho}V'\langle(\nabla\rho)^2\rangle\Gamma_W = S_W,$$

where $V' = dV/d\rho$. In the absence of a particle source and in stationary conditions the integration of this equation simply gives that the flux surface averaged particle flux is zero, that is $\Gamma_W = 0$. However, during a W accumulation phase, the stationarity condition is not necessarily satisfied. Therefore, in order to proceed with the present approach, which is not intended to describe the entire time evolution of the W density, but only to model two specific time slices, and since the time evolution of the W density is not directly known, we shall assume that the stationarity condition is applicable, and we shall verify *a posteriori* the error that this assumption implies. With this assumption, the condition $\Gamma_W = 0$ leads to the following equation for the normalized low field side logarithmic density gradient

$$\frac{R}{L_{nW}} = -\frac{RV_{WNEO} + RV_{WGKW}}{D_{WNEO} + D_{WGKW}} \quad (1)$$

The impact of the neglect of the time evolution of the W density in Eq. (1) can be estimated by considering the time evolution of the signal t_{19} of the central line of sight of the vertical SXR camera. Assuming that $n_W(\rho < 0.3, t) \propto t_{19}(t)$, we can estimate the impact of the time evolution of the W density on R/L_{nW} as

$$\left[\frac{R}{V'\langle(\nabla\rho)^2\rangle D_W n_W(\rho, t)} \int_0^\rho \frac{\partial n_W(\rho, t)}{\partial t} V' d\rho \right]_{\rho=0.3} \simeq \left[\frac{RV(\rho)}{V'\langle(\nabla\rho)^2\rangle D_W t_{19}(t)} \frac{dt_{19}}{dt} \right]_{\rho=0.3}. \quad (2)$$

The most critical step in the application of Eq. (1) is provided by the summation of the neoclassical and turbulent transport components. It is well known that the level of turbulent transport is particularly sensitive to local gradients, and, therefore, within the uncertainties of the measured gradients the predicted turbulent fluxes can vary substantially. In contrast, it is generally observed that the ratios between the fluxes of the different transport channels undergo more limited variations, which justifies

an approach in which the levels of all the turbulent fluxes (and therefore also of the turbulent transport of impurities) are rescaled in such a way that the predicted turbulent heat flux matches the anomalous part of the power balance heat flux [46]. In practice, the neoclassical and turbulent transport components are combined in order to obtain a prediction of the normalized logarithmic gradient of the W density in this form,

$$\frac{R}{L_{nW}} = -\frac{\frac{\chi_{i\text{an}}}{\chi_{i\text{NEO}}} \frac{RV_{W\text{GKW}}}{\chi_{i\text{GKW}}} + \frac{RV_{W\text{NEO}}}{\chi_{i\text{NEO}}}}{\frac{\chi_{i\text{an}}}{\chi_{i\text{NEO}}} \frac{D_{W\text{GKW}}}{\chi_{i\text{GKW}}} + \frac{D_{W\text{NEO}}}{\chi_{i\text{NEO}}}}. \quad (3)$$

In Eq. (3) the turbulent ion heat conductivity predicted by the GK calculations $\chi_{i\text{GKW}}$ is assumed to match the anomalous part of the ion heat conductivity $\chi_{i\text{an}} = \chi_{i\text{PB}} - \chi_{i\text{NEO}}$. Here $\chi_{i\text{PB}}$ is the power balance ion heat conductivity obtained by interpretive simulations with the JETTO transport code [47], whereas $\chi_{i\text{NEO}}$ is the neoclassical ion heat conductivity. The normalization to the ion heat conductivity used in Eq. (3) is appropriate for these cases, where the ion heat flux is dominant and, consistently, ITG instabilities have been found to dominate the linear spectrum.

Fig. 4 shows a summary of the results of the neoclassical transport calculations and allows a first analysis of the differences between the two time slices. Two transport relevant dimensionless quantities, the ratio $D_{W\text{NEO}}/\chi_{i\text{NEO}}$ and the ratio $RV_{W\text{NEO}}/D_{W\text{NEO}}$ are plotted in Fig. 4(a) and 4(b) respectively. We observe that the main difference between the time slices occurs inside $r/a = 0.4$. At 5.9 s, as a consequence of a slightly hollow main plasma density profile, the neoclassical W convection is directed outwards, whereas in the later phase, at 7.5 s, the central peaking of the main plasma density profile, as shown in Fig. 2, produces a strong inward convection close to the magnetic axis. We stress that in the case of the calculations which include the rotational effects, these transport coefficients are defined in relation to the LFS density profile. We notice that calculations in which the rotational effects (and in particular the centrifugal trapping) are neglected provide profiles of the convection to diffusion ratio $RV_{W\text{NEO}}/D_{W\text{NEO}}$ in the central region of the plasma which are very close to those obtained with the inclusion of the rotational effects, whereas they become significantly different approaching the edge. We have verified that the increasing difference between the convection to diffusion ratios computed with and without centrifugal effects with increasing minor radius is connected with the concomitant increase of the collision frequency. Indeed, a recent study shows that neoclassical transport is strongly affected by whatever type of poloidal asymmetry of the W density, and that the effect of temperature screening in the Pfirsch–Schlüter regime becomes weaker in the presence of asymmetries, leading to a reversal from outward to inward of the convection in the presence of a poloidal asymmetry [44]. This suggests that neoclassical models which do not include rotational effects can still be considered for an approximate estimate of this important ratio, at least in the core of low collisionality plasmas, but cannot be considered applicable in general. In contrast, and as is expected from past [41–43] and recent [45] analytical studies, a large difference is obtained in the ratio $D_{W\text{NEO}}/\chi_{i\text{NEO}}$ as a consequence of the inclusion of rotational effects, which strongly enhance both the neoclassical W diffusivity and convection (we notice also the reduction of this effect in the most central region of the plasma at 7.5 s, which is produced by a locally hollow

thermal Mach profile). In conclusion, from the standpoint of neoclassical transport, a significant difference can be identified between the profiles of RV_W/D_W inside $r/a = 0.4$ at the two time slices. This difference is a consequence of the different shapes of the background plasma density profiles in the central region, as shown in Fig. 2(b).

The W turbulent transport has been computed with the gyrokinetic code GWK [37,38] and the results are summarized in Fig. 5 and Fig. 6 for the two time slices 5.9 s and 7.5 s respectively. In the presence of rotation, a general expression for the turbulent radial particle flux of impurities is given by [25]

$$\frac{R\Gamma_{nZ}}{n_Z} = D_{NZ} \left(\frac{R}{L_{nZ}} + C_{ThZ} \frac{R}{L_{TZ}} + C_{UZ} u'_Z + C_{pZ} \right), \quad (4)$$

where centrifugal effects also impact the values of the transport coefficients [30]. Here $u'_W = -(R^2/v_{thW})d\Omega/dr$, and Ω is the toroidal rotation, which is assumed to be the same for all the ions, which we have verified to be appropriate at least inside $r/a = 0.8$. The linear growth rate γ and real frequency ω_r at the usual most unstable wave number $k_y \rho_i = 0.3$ are shown in Figs. 5 and 6. In both cases the most unstable modes are ITG, and in both cases unstable modes are found only outside $r/a = 0.2$, consistent with the JETTO result that the power balance ion heat conductivity approaches the computed neoclassical conductivity around $r/a \simeq 0.25$ and becomes even smaller inside, which indicates that, considering the uncertainties, ion heat transport is neoclassical in that region. Real frequencies and growth rates are very similar for the two time slices, as are the W transport coefficients, shown in Figs. 5(b) and Fig. 6(b) respectively. Consistent with the expected behaviour in ITG turbulence, the thermo-diffusion contribution $C_{ThW}R/L_{TW}$ (curve labelled ThD in the plots) is outward, whereas the roto-diffusion component $C_{UW}u'_W$, which in ITG turbulence is directed outward in the absence of centrifugal effects [46,48], can reverse direction and be directed inward (negative) due to the impact of centrifugal effects on roto-diffusion [30]. Finally, the pure convection component $C_{pW} = RV_{pW}/D_W$ is dominated by $E \times B$ compression, and is usually directed inward, but centrifugal effects add an outward directed component which can compensate and even reverse its sign [30]. The sum of all the off-diagonal contributions delivers profiles of the total convection to diffusion ratio RV_W/D_W which exhibit similar features at the two time slices (squares in Fig. 5(b) and Fig. 6(b)). The ratio RV_W/D_W is positive (directed outward) in the most central region, crosses zero around mid-radius, and it is directed inward approaching the edge region.

Having examined the neoclassical and turbulent transport contributions separately, we consider Eq. (3) in order to properly combine neoclassical and turbulent transport terms. The four terms of Eq. (3) are plotted in Fig. 7 and Fig. 8 for the time slices 5.9 s and 7.5 s respectively. Fig. 7(a) and 8(a) show the turbulent and neoclassical terms of the numerator (the convective components), whereas Fig. 7(b) and 8(b) show the turbulent and neoclassical terms of the denominator (the diffusive components). For direct comparison between neoclassical and turbulent terms, consistent with the justification for Eq. (3), GWK results are plotted with the normalizations included in Eq. (3), that is $D_{WGKW}/\chi_{iNEO} = (D_{WGKW}/\chi_{iGKW})(\chi_{ian}/\chi_{iNEO})$ and analogous expression for RV_{WGKW}/χ_{iNEO} . The ratio $(\chi_{ian}/\chi_{iNEO})(D_{WGKW}/\chi_{iGKW})$ appearing in the denominator of Eq. (3) becomes significantly larger than the corresponding

neoclassical term $D_{W\text{NEO}}/\chi_{i\text{NEO}}$ at $r/a > 0.5$, shown in Fig. 7(b) and Fig. 8(b). However, as a consequence of the enhancement produced by rotational effects, neoclassical transport dominates the central part of the plasma, and the neoclassical convection components $RV_{W\text{NEO}}/\chi_{i\text{NEO}}$, shown in Fig. 7(a) and 8(a), are nowhere negligible in these plasmas. Actually, they provide the dominant contribution, particularly in the central region $r/a < 0.3$, and determine the main differences in the predicted W behaviour between the two time slices. By summing the various terms, the radial profiles of R/L_{nW} at the LFS can be computed and are presented in Fig. 9(a). We observe that the sum of the various contributions delivers two LFS radial profiles of R/L_{nW} for the two time slices which display similar features outside $r/a = 0.4$, but which differ markedly inside $r/a = 0.3$. In the plasma region where strong accumulation is predicted at 7.5s, we have also performed a set of simulations in the W non-trace limit. These result in a slightly increased value of the predicted W logarithmic density gradient, as shown in Fig. 9(a).

At this stage, we have all the elements needed to estimate the impact of the neglected time evolution of the W density during the accumulation phase at 7.5 s in the calculation of the normalized logarithmic W density gradient R/L_{nW} . Using Eq. (2), and the experimental time evolution of the signal t_{19} and the predicted total diffusion coefficient of W, we obtain a contribution to R/L_{nW} which is of the order of 1, to be compared with values of $-RV_W/D_W$ which can exceed 100. We conclude that at least for the case which has been examined, the time evolution of the accumulation, while not completely negligible, is still slow enough to permit the present approach of modelling a single time slice as if it were in stationary conditions.

The two R/L_{nW} profiles shown in Fig. 9(a) can be integrated along the minor radius, considering a boundary condition at the LFS edge density which is taken from the experimentally determined LFS W density, as obtained by the diagnostic methods described in the next section. The two predicted LFS tungsten density profiles are plotted in Fig. 9(b). At 5.9 s, the centrally hollow W density profile is produced by the neoclassical outward convection generated by the transiently weakly hollow main plasma density profile, already shown in Fig. 2(b). At 7.5 s, the strong peaking of the W density profile, a signature of ongoing strong accumulation, is the direct consequence of the inward neoclassical convection produced by the central peaking of the plasma density profile in this later phase. From these results we can already conclude that the main qualitative difference between the two time slices is reproduced by the theoretical models. From the LFS profile of n_W shown in Fig. 9(b), by taking into account the poloidal asymmetry produced by centrifugal effects [52, 53], the 2D density distribution of W over the poloidal cross-section can be predicted. In practice, the 2D distribution of W density over the poloidal cross-section is reconstructed starting from the predicted LFS density profile $n_0(r)$, by including the impact of the profiles of the plasma toroidal angular velocity $\Omega(r)$ and the related computed background electrostatic potential $\Phi(r, \theta)$,

$$n(r, \theta) = n_0(r) \exp \left\{ -\frac{Ze\Phi(r, \theta)}{T(r)} + \frac{m\Omega^2(r)}{2T(r)} (R(r, \theta)^2 - R_0(r)^2) \right\}. \quad (5)$$

The predicted 2D W density distributions are presented in the next section, and will allow a direct quantitative comparison with the experimental W density obtained by the experimentally reconstructed W densities.

4. Comparison between experimental results and theoretical predictions

In this section, the two diagnostic techniques for the 2D W density are described and the comparisons between the theoretically predicted W density results and the experimental results are presented. Since the 2D W density is not directly measured by any diagnostics, in order to reach the possibility of a direct comparison between theory and experiment additional steps have to be undertaken. From a general perspective, these can be performed in two directions.

One approach is to compute a set of more or less directly measured quantities, starting from the theoretically predicted W transport coefficients or the predicted 2D W density. To this end, it is practical to apply an impurity transport code and to perform impurity transport simulations in which plasma profiles are fixed from experiment and impurity profiles are calculated utilizing transport coefficients as predicted by theory, in order to obtain results which can be directly compared with a set of measured quantities, such as line integrated signals of SXR emission, radiated power and Z_{eff} profiles. In case of disagreement, the impurity transport simulations can be iterated adjusting the transport coefficients until a good match between measured and simulated quantities is reached. Thereby, this method not only allows the computation of measured quantities from the theoretically predicted transport coefficients but can also yield the best-fitted W density profile to be compared with theory. In case of transient transport experiments, it also yields the empirically determined W transport coefficients, diffusion and convection, separately, which can be also compared with theory. In the relatively stationary conditions of the plasmas considered here, however, only the convection to diffusion ratio is meaningful and will be considered for comparisons.

The other approach instead is developed in the opposite direction. It makes a direct interpretive use of the SXR measurements, without involving transport, and deduces the 2D W density from the tomographic reconstruction of the SXR emission after having subtracted the component not due to W [31]. The 2D W density yielded by this 2D SXR W density diagnostic can then be compared with the theoretical predictions.

In this paper, both approaches have been applied to the JET hybrid scenario discharge #82722. Clearly, both approaches require the calculation of the Bremsstrahlung from light impurities and hydrogenic ions, assuming that they display negligible density asymmetry (as it is the case at the observed plasma rotations) in order to identify the contribution to the SXR emission which is solely produced by W. This implies the need for a sufficiently precise absolute calibration of the SXR signals. In this work, both diagnostic methods have used the same calibration of the JET SXR cameras. A dedicated study has revealed that absolute calibration requires signals from the different JET SXR cameras to be multiplied by factors between 1.5 and 2.0 in order to be consistent with calculated Bremsstrahlung levels in plasmas in which W is

absent (specifically for the studies presented in this paper, JET SXR cameras have been multiplied by the following factors, cameras T and V by 1.7 and camera H by 1.5).

The next two subsections will describe the two methods in more detail. Then the comparisons between the results of these independent diagnostic analyses are presented, which give indications on the level of uncertainties associated with the experimental determination of the shape of W density distribution, and on the absolute concentration levels, at least in the range of plasma parameters present in JET hybrid scenario plasmas. Both results are also compared with the theory predictions described in Sect. 3.

4.1. Determination of W density via JETTO/SANCO impurity transport simulations

The 1D JETTO/SANCO transport code [32] has been used to perform impurity transport simulations of the JET-ILW hybrid scenario discharge # 82722. This code can be used in both predictive and interpretive mode. In the present application, we have applied an interpretive approach, but we have used the theoretically predicted impurity transport coefficients as initial condition for the interpretive procedure applied in order to identify the solutions which best fit a large set of raw data. The simulated impurities are W and Be. Ni has also been added as third impurity, in order to estimate the maximum Ni content which remains compatible with the measurements and has been found to be practically insignificant. For this reason, in this section only the W and Be simulations are presented. The interpretive modelling approach considers plasma kinetic profiles of electron density, electron and ion temperature and toroidal rotation velocity which are kept fixed from measurements, whilst the impurity profiles are predicted using diffusion and convection velocity profiles. In the present approach the theoretically predicted flux-surface averaged (FSA) W transport coefficients are used to initialize the procedure. Starting from initial coronal distribution, the code computes the radial profile of the density of each ionized state (74 for W and 4 for Be) taking into account the effect of transport, from the theoretically predicted transport coefficients, and assumed that these are same for each ionized state of one impurity. While this assumption is not theoretically founded when the charge variation is considered over the entire window for W (from 1 to 74), this approach can still be justified “a posteriori” by the result that at a given electron temperature only a limited number of ionization states is significantly populated, within a small charge window, in which the transport can be practically considered to be the same for each ionized state. This also justifies the modelling approach used in the theoretical calculations, which considers a single averaged charge state at each radial location (and therefore electron temperature). The result provides a distribution of W ionized states which remains very close to the coronal equilibrium. The Be transport coefficients have been constructed according to the simple prescription [54] that $D_{Be} = 0.5\chi_{i,PB}$ and $RV_{Be}/D_{Be} = R/L_{ne}$, where R/L_{ne} is the measured electron density logarithmic gradient normalized to the major radius. The absolute amount of Be has been tuned in order to match the line integrated Z_{eff} from visible spectroscopy. The W transport coefficients and W influx are instead started from the profiles which are theoretically predicted by the GKW and NEO simulations and, if needed, adjusted iteratively so that the predicted SXR emission matches the line integrated SXR emission

from the 3 SXR cameras with vertical and horizontal views [39]. In order to compare the 1D simulation with the 2D SXR measurements, two postprocessors have been used, UTC [33] and SXRPY [34], which allow the reconstruction of the 2D W density distribution over the poloidal cross section which is consistent with the SANCO 1D W density, taking into account the W density poloidal inhomogeneity produced by centrifugal effects, considering the toroidal rotation profile from CXRS measurements, and using Eq. (5). From the 2D density distribution consistent with the 1D SANCO result, both postprocessors calculate the SXR emission (Bremsstrahlung continuum and line radiation, using ADAS atomic data [55] and taking into account the effect of the Be filters) and perform line integrals according to the geometry of SXR cameras and EFIT reconstructed equilibrium using polarimetry data. The procedure is then iterated by adjusting the impurity transport coefficients in SANCO in order to best fit the measured SXR signals. The consistency is also checked against the line integrated signals of the radiated power density obtained by the measurements of the JET bolometers [56]. Consistency with vacuum ultraviolet (VUV) (for W) and CX (for Be) spectroscopy is also verified.

The levels of agreement of the JETTO/SANCO interpretive simulations with the SXR line integrated signals for the two time slices of shot 82722 are presented in Fig. 10. The comparison between the JETTO/SANCO and UTC simulations of the line integrated signals of the horizontal camera of the bolometric diagnostic with the corresponding actual measurements is shown in Fig. 11, whereas Fig. 12 shows the consistency of the JETTO/SANCO results with the experimental line averaged values of Z_{eff} .

The adjusted empirical profiles of RV/D for W which allow us to obtain this level of consistency are shown in Fig. 13. These are directly compared with those predicted using GKW and NEO and presented in Section 3 (note that transformations from the LFS values shown in Fig. 7 and in Fig. 8 to FSA values have been performed, following the transformation rules presented in the Appendix). The shaded region in Fig. 13b shows the variation of the RV/D profiles within which equally good matches of the experimental measurements are obtained. Fig. 13a demonstrates that for the case at 5.9 s the theoretically predicted profile of RV/D directly provides the best match of the measured quantities which are fitted by the JETTO/SANCO interpretive simulation. In contrast, for the case at 7.5 s an additional adjustment of the profiles is required in the region close to the magnetic axis in the JETTO/SANCO interpretive modelling. The disagreement might be partly connected with uncertainties in the background density and ion temperature profiles (the empirically determined values of RV/D can be matched if the electron density logarithmic gradient is decreased by 20% to 30% and the ion temperature logarithmic gradient is increased by 50% to 30%, dotted line in Fig. 13b). In addition, it has to be expected that, in the presence of very strong gradients of the W density profile, conventional neoclassical theory (which is based on an ordering on the poloidal Larmor radius) becomes less accurate. We note however that while the difference in the convection to diffusion ratio close to the axis at 7.5 s is relatively large (more than a factor 2), this has limited impact on the reconstructed W density profiles, since in both cases we obtain the consistent result that the W density profiles

are extremely peaked close to the magnetic axis. Therefore, from this first comparison between experimental results and theoretical predictions presented in Fig. 13 we obtain indications of a quantitative agreement.

The 2D mapping of the W density (Be is poloidally symmetric) and corresponding horizontal cuts at the magnetic axis height ($Z = Z_{mag}$) are shown in Fig. 14 and Fig. 15 in Subsection 4.3, where these experimental results are compared with those obtained by the SXR 2D W density diagnostic (described in the next subsection) and by the NEO and GKW predictions.

4.2. Determination of W density via a 2D SXR W density diagnostic

This method is based on the direct deconvolution of the SXR signals with a model-based functional form of the W density dependence on the poloidal angle [31]. The Bremsstrahlung contribution from all low- Z ion species is subtracted from the measured SXR signals, where the same absolute calibration factors used in the JETTO/SANCO analysis are applied. The residual SXR emission is attributed to W, and is deconvoluted assuming the following functional form

$$n_W(\rho, R) = n_W(\rho, R_0) \exp[\lambda(\rho)(R^2 - R_0^2)], \quad (6)$$

which reproduces the general form of the 2D distribution of W density in the presence of centrifugal effects Eq. (5) [52, 53]. Here $n_W(\rho, R_0)$ and $\lambda(\rho)$ are two arbitrary 1D functions which are adjusted in order to match the residual emission of the SXR signals. We notice that the function $\lambda(\rho)$ is directly connected with the toroidal rotation velocity profile of the plasma, and its determination with this method, assuming W only, has been verified to be consistent with the CXRS measurements. The good quality of the fit ensures the capability of this description to correctly capture the actual poloidal asymmetry of the W distribution. This also allows us to verify that the residual SXR emission produced by heavy impurities can be fully ascribed to W, since other impurities would imply different levels of toroidal velocities, inconsistent with the CXRS measurements. In order to obtain absolute values of the W density, the T_e dependent SXR cooling factor is required. In contrast to the previous method, where the ADAS data have been applied, this diagnostic technique utilizes adjusted atomic data. The SXR cooling factor has been derived by comparing the W density calculated from total radiated power and line-integrated VUV spectroscopy data with core SXR brightness in plasmas with varying levels of on-axis ICRF heating. This procedure assumes coronal equilibrium and a flat W density profile. The assumption of coronal equilibrium is supported by the results obtained by the JETTO/SANCO simulations.

In general, both these methods can be applied provided the electron temperature is high enough (typically $T_e > 1.5$ keV) and the W concentration large enough ($C_W > 10^{-5}$), to ensure that the detected SXR radiation is large enough and mainly produced by W (which reduces the uncertainties given by the subtraction of the plasma background SXR emission). Finally, we note that in the present form both methods are well suited to describe an out-in asymmetry, as typically provided by centrifugal effects, but require to be extended to describe also in-out asymmetries produced by

ICRF heating [20, 57, 58], as well as to describe possible up-down asymmetries.

4.3. Comparison between experimentally reconstructed and theoretically predicted 2D W density distributions

The experimental 2D W density obtained from the 2D SXR W density diagnostic and the JETTO/SANCO and SXRPY analysis are shown in Fig. 14(a,b) and Fig. 14(c,d) respectively. These are directly compared with the theory-based modelling results in Fig. 14(e,f). The figure clearly shows the W localization at the LFS at 5.9s due to centrifugal trapping in the presence of a hollow LFS W density profile, and an extreme central peaking at 7.5 s, which is produced by neoclassical accumulation. The agreement between the experimentally reconstructed W densities obtained with the two diagnostic techniques is extremely good, as also shown in Fig. 15, where horizontal cuts at the height of the magnetic axis are plotted. Representative error bars of the experimentally reconstructed density are also presented. Of course, the absolute concentrations derived from the experimental analyses and shown in Figs. 14 and 15 are affected by larger error than the shapes of the W density 2D distributions and profiles. Still we can estimate that their uncertainties are below a factor 2, as supported by the agreement found with these two independent diagnostic methods. At 5.9 s the central W concentrations is negligible but the off-axis peak amounts to $n_W/n_e \sim 10^{-4}$, while at 7.5 s the central W concentration reaches values $n_W/n_e \sim 10^{-3}$. Whilst the early phase is compatible with good plasma performance and enhanced confinement, the central accumulation is always associated to degraded performance. In contrast, the Be concentrations obtained by the JETTO/SANCO analysis exhibit a more limited variation, from 1.5% at 5.9s to 3.5% at 7.5 s.

As also demonstrated in Figs. 14 and 15, the theoretical predictions closely reproduce the 2D density distributions, and are found in quantitative agreement within the respective uncertainties. We note that the agreement between theoretical predictions and experimental W densities has to be sought only in the shape of the W density 2D distributions and profiles, but not on the absolute values, since, as already mentioned in Section 3, the theoretical modelling takes the absolute value of n_W at the boundary $r/a = 0.85$ from the experiment. The impact of using the trace or non-trace limit for the prediction of the central W density during the W accumulation phase is illustrated in Fig. 15(b).

Since both the modelling and the SXR interpretive W density diagnostic assume that the only source of asymmetry is connected with centrifugal effects, we also consider SXR tomographic inversions of the SXR signals, which are performed without any assumption on the type of the asymmetry. These tomographic inversions are applied to the entire SXR emissivity, without any subtraction of background Bremsstrahlung emission, and use the flux surface geometry as a constraint for the preferential smoothness [59]. Assuming that most of this emission is produced by W, as it turns out to be for these plasmas, and therefore neglecting the background contribution to the SXR emission from the rest of the plasma, these tomographic inversions, shown in Fig. 16(c,d), can be qualitatively compared with the prediction of SXR radiation

obtained from the predicted W density considering appropriate W cooling factors, which include the impact of the Be filter present in the JET system, shown in Fig. 16(a,b). This somewhat more qualitative comparison confirms the general agreement between theoretical predictions and experimental observations, and also allows the examination of the possible additional asymmetries which have not been accounted for in the 2D W density SXR interpretive diagnostic. We notice that also in Fig. 16(c) the main asymmetry is an out-in asymmetry, with a location and size which is well predicted by the modelling, consistent with the result of the comparison in Figs. 14 and 15. We also observe that a small up-down asymmetry of the SXR emission is present in the tomographic inversion. This might suggest that this small up-down asymmetry is produced by ion-impurity friction [43,60], which has not been taken into account in the present modelling. The ion-impurity friction parameter g (as defined in Eq. (24) of Ref. [43]) is smaller than 0.05 for $r/a \leq 0.70$ (and smaller than 0.03 in the region of maximum brightness of the SXR emission, $r/a \simeq 0.6$), and increases rapidly only outside, exceeding unity at $r/a = 0.83$. Whether this level of friction is consistent with the observed small up-down asymmetry will be considered in a separate study, where up-down asymmetries will be analysed in a more systematic way in order to examine SXR tomographic inversions of a larger amount of plasmas at different currents and collisionalities, also in order to clarify whether this (small) up-down asymmetry is an artefact of the tomography. Several diagnostic set-up complications could potentially cause a spurious up-down asymmetry, in particular the fact that the horizontal and vertical detectors have different spectral sensitivities and different toroidal positions and the fact that smoothness is imposed to be higher along flux surfaces, but inner flux surfaces may have considerable position error. The investigation of the physics of up-down asymmetries and in particular whether the plasma exhibits non-neoclassical levels of asymmetry, as recently documented in Alcator C-Mod [61], is not only important from a physics perspective, but also from a practical one. In ITER core ion temperature and toroidal rotation velocity will be measured by imaging crystal spectrometry on one half of the poloidal cross-section. As shown in [62], an unaccounted up-down emissivity has a large impact on the derived values of ion temperature and rotation.

In summary, the interpretive analysis of the SXR signals identifies W as the impurity being responsible for the observed differences in the SXR emission between the two time slices. At 5.9 s, the bean shaped emission is localized off-axis at the LFS, and is produced by a strongly hollow LFS W density profile in combination with strong centrifugal effects. At 7.5 s, the strongly peaked emission, which is completely localized on-axis, is produced by a centrally peaked W density profile, which is indicative of ongoing central W accumulation. The results obtained from the modelling of neoclassical and turbulent W transport with the NEO and GKW codes closely reproduce the features observed in the experiment, and allow us to identify neoclassical convection in the central region of the plasma as the dominant transport mechanism being responsible for the different behaviour of W at the two time slices. The change in neoclassical convection is directly produced by the transient behaviour of the main plasma density profile, which is hollow in the central region in the initial part of the high power phase of the discharge, but which develops a significant density peaking in the later phase. The plasma region

which determines the W accumulation is very close to the magnetic axis, practically inside $r/a = 0.3$.

Finally, it is of interest to compare the experimentally reconstructed W densities with those which are obtained neglecting the centrifugal effects in the modelling. The centrifugal effects can be considered to enter in two ways. The first way is by affecting the equilibrium density in the direction parallel to the magnetic field lines, and therefore by developing a poloidal asymmetry connected with the centrifugal trapping. The second way is by affecting the radial transport. In Fig. 17 the experimentally reconstructed W density as a function of major radius at the magnetic axis height is compared with the theoretical predictions obtained neglecting centrifugal effects on both the equilibrium poloidal asymmetry and the radial transport. While the essential feature of the presence or absence of W accumulation is still captured by the theoretical modelling, the predictions of course cannot reproduce the poloidal asymmetry, and do not reproduce as closely the profiles even at the LFS. In Fig. 18 we present the results of a hybrid (and not consistent) approach, in which the centrifugal effects are neglected in the calculation of the radial transport, but are kept in the poloidal mapping. In this approach, the result of the NEO and GKW calculations, performed switching off all centrifugal terms, are interpreted as FSA densities, which are then mapped over the 2D poloidal cross-section according to Eq. (5). In this case the theoretical results follow more closely the experimentally reconstructed profiles, and agree with the results obtained by considering the full and consistent model, presented in Fig. 15. The good agreement obtained with this simplified method is the direct consequence of the fact that in these cases the centrifugal effects are not found to affect significantly the neoclassical RV_{NEO}/D_{NEO} ratio, as already shown in Fig. 4. While this simplified and inconsistent approach might be applied with models which do not allow the consistent inclusion of centrifugal effects, it should be underlined that the agreement found on these two cases is deceptive and should not be considered to be generic, particularly for applications to rotating plasmas at higher collisionality.

5. Generality of the results, analysis of database of hybrid discharges and role of MHD activity

In this section, the generality of the conclusions drawn from the analysis performed so far is investigated. In order to proceed with the analysis, a first step is to build a simple proxy for the W density peaking in the central region of the plasma, which can be used for the study of many discharges. To this end, we use the line integrated signals of a SXR vertical camera and we consider two lines of sight (LOS), one which passes through the magnetic axis (and which will be identified as t_{19}) and one which passes off-axis and which is tangent to the magnetic surface with $r/a = 0.4$ (and which will be identified as t_{25}). The ratio t_{19}/t_{25} can be considered to give information on the level of central peaking of the W density profile in the central region of the plasma. A better proxy for the actual W density peaking in the center can be defined

as $p_W = (t_{19}/t_{25})/(l_{19}/l_{25})/(n_e(0)/n_e(0.4))$, where we have normalized the ratio of the two signals of the SXR LOS to the corresponding chord lengths of the LOS (l_{19} and l_{25} respectively) and to the ratio of the electron densities at the magnetic surfaces to which the LOS are tangent (practically the magnetic axis for the central LOS t_{19} , and $r/a = 0.4$ for the peripheral LOS t_{25}). The use of SXR signals is appropriate, since, in the time windows of the discharges that we have considered, the electron temperature in the core region regularly exceeds 2 keV, and therefore remains above the threshold temperature below which the W emitted power in the SXR range becomes extremely low. Moreover, the use of a vertical camera is appropriate in the case of dominant out-in asymmetries as in these hybrid scenario plasmas.

The first aspect that we consider is the fact that the plasma region which is relevant in determining the accumulation process is very close to the axis. To this end, we examine the time evolution of two other discharges in hybrid scenario. The first, shot #83532, similar to shot #82722, exhibits W accumulation in the later part of the high power phase. The second, shot #82527 does not display W accumulation (for reasons which will be at least partly clarified later).

In Fig. 19, the time evolution of the ratio t_{19}/t_{25} of these two shots is shown together with the time evolution of the normalized logarithmic density gradient R/L_{ne} at various radial locations. Consistently with the results obtained from the analysis of shot #82722, the accumulation occurring in shot #83532 is concomitant with an increase of R/L_{ne} in the center ($r/a = 0.15$), whereas shot #83527, which does not exhibit accumulation, does not exhibit an increase in the central value of R/L_{ne} either. It is also of interest that the time traces of R/L_{ne} differ only in the very center, but outside $r/a = 0.3$ they are almost identical. This observation is consistent with the conclusion drawn on the basis of the modelling results, that the plasma region which is relevant in determining W accumulation is very close to the magnetic axis. It is also of interest to observe that, after the NBI switch on, and the consequent transition to H-mode, the values of R/L_{ne} have a rapid drop and become transiently negative, particularly around $r/a = 0.4$, which is a common feature of these hybrid scenarios. This feature was already observed in shot #82722 (Fig. 1 and Fig. 2).

Hollow main plasma density profiles are favorable to avoid neoclassical accumulation, but this condition is only transient, and eventually in these discharges the main plasma density peaks in the center. In almost the totality of cases, W is also observed to peak, following the behaviour of the electron density. This suggests an important role of neoclassical W transport in the accumulation process, consistent with the theory modelling results presented in the previous section. The comparison between conditions which lead to W accumulation with those in which W accumulation is not observed reveal that the critical radial window in which the peaking of the main plasma density profile is related to W accumulation is inside $r/a = 0.3$.

This also suggests that the time history of the W accumulation should show some level of correlation with a parameter which describes the strength of the neoclassical inward convection in the central region of the plasma. To this end, we consider the local parameter $R/L_{ne} - 0.5R/L_{Te}$ at $r/a = 0.15$ which is roughly proportional to a simple analytical estimate of the neoclassical pinch to diffusivity ratio of W [63] (since the main

ion density and temperature are not available on a regular basis for these discharges, R/L_{ne} and R/L_{Te} , as measured by the HRTS system, are used in place of R/L_{ni} and R/L_{Ti}). In Fig. 20 the time evolution of the proxy p_W for the central W peaking is plotted against the local parameter $R/L_{ne} - 0.5R/L_{Te}$ evaluated at $r/a = 0.15$. The large majority of the discharges follow more or less the same curve in this space of variables, which provides strong indication that the dominant role of central neoclassical convection in determining the behaviour of these discharges is generic in the JET-ILW hybrid scenario, consistent with the result which has been obtained with the modelling of the previous section, which was specific to discharge #82722. An interesting aspect of the result presented in Fig. 20 is provided by the behaviour of shot #83527, which is the only case in this database of discharges (and the only one we have been able to find) in which the high power phase does not eventually lead to W accumulation. The evolution of this discharge is plotted with large diamonds in Fig. 20, and it is the only one for which the W peaking proxy p_W saturates close to unity. Correspondingly, the parameter $R/L_{ne} - 0.5R/L_{Te}$ on the x-axis also saturates at values which remain close to zero. This specific observation appears to corroborate the proposed critical role of the central density peaking of the main plasma as the main cause for the W central accumulation. When the density does not peak, accumulation is not observed. This observation also raises the question of why in this specific discharge the electron density does not develop a strong central peaking, in contrast to many other cases. Fig. 19(b) shows that in the discharge #83527, R/L_{ne} at $r/a = 0.15$ remains practically clamped to zero after having recovered from the initial hollow phase. A similar behaviour is also observed for the electron temperature profile. A closer inspection of the time behaviour of the electron density and temperature gradients in the central region (inside $r/a = 0.3$) of that discharge shows that they are both practically clamped to zero after 6.8 s (that is 2.2 s after the NBI switch on in Fig. 19). The similar behaviour of both the central electron temperature and central electron density suggests us to analyse the MHD activity of this discharge, and adds a new element to the present study, that is the role of MHD modes on the background plasma as well as directly (or indirectly) on the W behaviour. The analysis reveals that this discharge is characterized by an $n = 1$ mode of significant amplitude starting from 6.0 s. The mode is identified of kink type in the initial phase, but it moves into tearing type shortly after 7.0 s. Thereby, it appears that, at least in this specific case, the presence of this $n = 1$ mode is beneficial with respect to the W behaviour, since it keeps the central plasma kinetic profiles flat, and prevents the development of W central accumulation. Nevertheless, this mode remains detrimental for the global confinement, since in this discharge the onset of this $n = 1$ mode leads to a further drop of the total plasma stored energy. In fact, β_N and H_{98y} , which in the early times of the high power phase reached values above 3.0 and 1.2 respectively, drop to values around 2.9 and 1.15 before the onset of the tearing mode, and reach values around 2.7 and below 1.05 in the presence of this mode.

An $n = 1$ mode is usually present in most discharges since in the early phase, alternating phases of kink type with phases of tearing type often terminated by a sawtooth crash. The role of sawtooth crashes is well exemplified by the time evolution of discharge #82722. In Fig. 21 the $n = 1$ mode amplitude and spectrogram in correlation

with central SXR emission and central electron density peaking are shown. When W is centrally peaked, the beneficial effect of crashes in expelling W from the centre is evident. Less obvious is to discriminate the effect of the $n = 1$ tearing mode phases. The correlation in time between electron density peaking and central SXR emission suggests that neoclassical transport always remains the driving term for accumulation. The $n = 1$ mode can possibly be beneficial by flattening the electron density profile, as it seems around $t=6.2$ s ($n = 1$ grows and electron density peaking slowly decreases together with central SXR, similarly to what is likely taking place in shot #83527), whilst later it does not seem to play a role until it culminates into a crash. It is also to be noted that the W accumulation process can be repeated in cycles, with central MHD crashes taking W outwards and flattening the electron density profile, and the electron density peaking again after the crash, leading again to the accumulation of W in the centre.

In conclusion, the present analysis suggests that the impact of the $n = 1$ mode on the W behaviour is often beneficial and can be both direct (by flushing out W with sawtooth crashes) as well as indirect, by impacting the background plasma density profile and therefore affecting the role of the neoclassical convection. However such a role of the $n = 1$ mode is not observed in all of the discharges [5], and further studies are required to better clarify the impact of $n = 1$ activity on the W behaviour in different conditions.

A complicated interplay between MHD activity and neoclassical transport also appears to be the source of the impact of higher n mode activity, in particular neoclassical tearing modes (NTMs), on the W behaviour. Some of these plasma discharges in hybrid scenario develop NTMs ($3/2$, $4/3$ or $5/4$), and in some cases interesting correlations in time are observed between the onset of the NTM and an increase in the peaking rate of W , or even the initiation of the accumulation process. An example is shown in Fig. 22. The initial rise of core W (central SXR LOS t_{19} in Fig. 22), in correspondence to the electron density peaking, is followed by the onset of the NTM, which further accelerates the accumulation process. Such a strong impact of NTMs on the W behaviour appears to be in contrast with the result of Fig. 20, which suggests that the neoclassical transport is the sole relevant drive of the accumulation (more than half of the discharges plotted in Fig. 20 have NTMs). In order to reconcile these two experimental evidences, we speculate that NTMs impact the W behaviour through an unfavorable interaction between the neoclassical transport and the development of an island, when the island appears in the presence of a hollow LFS density profile of W (like that observed and predicted at 5.9 s in shot #82722). Our hypothesis is that in these conditions, the impact of the island is to move W rapidly inward, into a more central region where the neoclassical transport is more unfavorable and can more efficiently lead to accumulation. In contrast, when the island appears in the presence of a LFS density profile of W which is already centrally peaked, the island does not have any significant impact on the time evolution of the W accumulation (or can even be beneficial to slow down the accumulation process). These two conditions are exemplified by two discharges which feature the onset of a $3/2$ NTM. The time evolution of the central and peripheral LOS signals of the SXR vertical camera of these shots are shown in Fig. 23. In shot

the NTM appears when the LFS W density profile is hollow (as indicated by the SXR signal t_{25} of an off-axis LOS being greater than the central SXR signal t_{19} in Fig. 23a), whereas in shot #83520 the opposite conditions occur, the 3/2 NTM appears when the LFS W density profile is peaked ($t_{19} > t_{25}$, Fig. 23c). Consistent with our hypothesis, in the first case a dramatic increase in the W peaking rate occurs after the onset of the NTM (Fig. 23b), whereas in the second case, after a short transient phase, the W accumulation rate is roughly the same as before the NTM appearance (Fig. 23d). In order to further support this hypothesis on the interplay between NTMs and neoclassical transport, we extend the investigation performed on the impact of the appearance of NTMs on the SXR signals in shots #83422 and #83520 to all of the JET-ILW hybrid scenario discharges featuring NTMs. The result is summarized in Fig. 24, where on the y-axis the the W peaking rate (estimated simply as $d \log(t_{19}/t_{25})/dt$) after the appearance of the NTM divided by the peaking rate before the appearance of the NTM is plotted as a function of the proxy of the W peaking p_W evaluated at the appearance of the NTM. Slopes in the bottom plots of Fig. 23 (dashed lines) show examples of the fits by which the peaking rates $d \log(t_{19}/t_{25})/dt$ are estimated in all of the discharges. This investigation confirms that in the cases where the NTM appears in the presence of a centrally peaked W LFS density, small changes in the W peaking rate are observed. In contrast, when the W LFS density is hollow, the change in peaking rate can be extremely large, in agreement with our working hypothesis. While this result does not provide a conclusive validation, it can be considered interesting evidence in support of this hypothesis, which motivates further experimental and theoretical investigation on the impact of islands on the 2D distribution of the W density, particularly in conditions of locally strongly hollow LFS W density profiles.

6. Conclusions and outlook

The behaviour of W in JET-ILW H-modes in hybrid scenario has been investigated from the experimental standpoint and modelled with a combination of neoclassical and turbulence codes. The W behaviour in this scenario is mainly determined by the corresponding transient evolution of the bulk plasma density profile. Early in the high power phase of the discharge, the electron density profile is hollow, and the W density exhibits a bean shaped off-axis LFS localization produced by centrifugal effects in the presence of a hollow LFS W density profile. At later times, concomitantly with the development of the central peaking of the electron density profile, W starts to accumulate in the center. Neoclassical DK (with the code NEO) and linear GK (with the code GKW) calculations of W transport during an early and a late time-slice of the high power phase of a representative hybrid scenario discharge reproduce these features of the W behaviour, as observed in the experiment. The theoretical predictions of the 2D W density over the poloidal cross section agree quantitatively with the reconstructions of the 2D W density distribution obtained by two independent diagnostic analyses, one based on the JETTO/SANCO package [32] interpretive modelling of impurity transport combined with post-processing codes UTC and SXPY, and the other based on a direct SXR 2D W density diagnostic [31]. The combination of experimental analysis and

theoretical modelling indicate that W accumulation in the core is mainly determined by neoclassical transport in the central region of the plasma ($r/a < 0.3$), and is the consequence of the strong neoclassical pinch produced by the peaking of the bulk plasma density profile very close to the magnetic axis. This conclusion is confirmed by the analysis of a dataset of hybrid scenario discharges, where the time evolution of a proxy of the W peaking is found to be highly correlated with a simple analytical estimate of the neoclassical pinch to diffusion ratio in the center ($r/a \simeq 0.15$). The investigation of the physical reasons for the peaking of the main plasma density profile is beyond the scope of the present work. Analysis and modelling carried out so far [64] provide strong indication that this is connected to the impact of the NBI particle source in the presence of relatively low density and low particle diffusion in the innermost region of the plasma. Operation which tends to reduce the impact of the central NBI particle source, due to reduced NBI power fraction and/or beam voltage, the use of more tangential beams, and higher density, should allow the plasma to develop a reduced density peaking close to the magnetic axis and consequently to avoid, or at least delay and slow down, the W accumulation process. The analysis of different plasma scenarios in different parameter domains should allow us to shed more light on the physics behind the peaking of the main plasma density close to the magnetic axis in the near future.

In some discharges, the appearance of MHD activity is observed to significantly impact the time evolution of the W behaviour. NTMs are observed to accelerate, or even initiate, the accumulation process, but not in all of the discharges in which they appear. It is suggested that this is a consequence of an interplay between the appearance of an island and the strong localized gradients of W density developed by neoclassical transport. When NTMs appear while the LFS W density profile is hollow, they can produce a rapid displacement of a significant amount of the off-axis LFS localized W toward a more internal region where neoclassical transport is more unfavorable, with consequent faster accumulation. When NTMs are triggered in conditions in which the W density profile is already centrally peaked, their appearance is not observed to impact significantly the time evolution of the accumulation process. These observations motivate theoretical investigation of the impact of an island on W transport in the presence of hollow or peaked W density profiles. Also the role of more central $n = 1$ modes deserves further investigation. In some cases there is clear evidence that these modes are beneficial in avoiding W accumulation (although perhaps not in keeping the high confinement). It is proposed that this occurs both directly, due to the impact of the modes on W density, and indirectly, due to the impact on the main plasma profiles (in particular the flattening of the central density).

From the modelling standpoint, this work reports the first ever attempt at validation of the theoretical prediction of the 2D W density over an extended radial domain of the poloidal cross-section. While the results are encouraging, further work is required in order to explore other parameter domains (particularly at different collisionalities, relevant for neoclassical transport), and in the presence of additional poloidal asymmetries, due to minority species produced by auxiliary heating systems, like ICRH. We note that also the pressure anisotropy of beam ions can be expected to affect the background electrostatic potential and to produce an additional source of

poloidal asymmetry in the W density. This has however been neglected in this work, under the assumption that in the presence of strong rotation and absence of ICRH, the poloidal asymmetry is dominated by centrifugal effects, since the pressure anisotropy and the concentration of beam ions are relatively small. The validity of this assumption should however be verified in the future with more complete calculations, which also take this effect into account [70].

This work also leads to the realization that neoclassical transport is strongly increased by rotational effects (by more than one order of magnitude in the center at typical rotation levels of NBI heated plasmas). While this effect was known from past theoretical studies on neoclassical transport [41–43], its implications have not been fully considered in the analysis of heavy impurity transport so far. In particular, it implies that the neoclassical diffusion coefficient of heavy impurities in rotating plasmas, which display significant W density out–in asymmetry, is much larger than the prediction of models which exclude rotational effects (e.g. codes like NCLASS [71] or NEOART [72]). This also implies that at least some of the past conclusions on the irrelevance of neoclassical transport for heavy impurity transport should be revised. In fact, many of these conclusions were based on the comparison of the experimentally observed fast time scales or the experimental estimates of high values of diffusivity with the predictions of small neoclassical diffusivities given by models which do not include rotational effects, and which predict much smaller neoclassical diffusivities than a model in which rotational effects are consistently included. More in general, whatever type of W poloidal asymmetry is predicted to strongly affect the neoclassical transport [44,45]. Neoclassical transport is strongly enhanced in the presence of strong out–in or in–out asymmetry, but can be strongly reduced in the presence of weak in–out asymmetries [44]. This motivates the development of consistent models which quantitatively account for these effects, in order to extend the modelling also to other sources of W poloidal asymmetries, such as in–out asymmetries induced by the presence of ICRH minority ions.

The role of central electron cyclotron heating (ECH) has been recognized as a very efficient tool in controlling W transport accumulation in ASDEX Upgrade [10]. This effect has usually been explained by an increase of the central W diffusivity as a consequence of transport being driven turbulent up to the plasma center by localized central auxiliary heating, as demonstrated in specific Si ablation experiments in ASDEX Upgrade [9], where the central diffusivity of Si was measured to increase by about a factor 3. While an increase of this size is certainly important to reduce the impact of the W neoclassical convection, it appears that in rotating plasmas this increase alone might not be sufficient to compensate the W neoclassical convection, which is strongly enhanced by rotational effects. Central ECH is regularly observed to reduce the plasma rotation [66], which is beneficial also in reducing the magnitude of the neoclassical rotational enhancement. However the present analysis of JET–ILW hybrid plasmas suggests that an additional beneficial effect of central ECH (as observed in ASDEX Upgrade) is to increase the central main plasma diffusivity and flatten the main plasma density profile very close to the magnetic axis (where no radially resolved measurement of the density profile is available in ASDEX Upgrade) even in conditions where central

ECH is observed to peak the electron density profile in the confinement region [46,65,66].

For the ITER standard scenario, the present analysis suggests that it is critical to consider the shape of the density profiles of the bulk ion species close to the magnetic axis. The plasma density will likely develop a transient behaviour featuring centrally hollow density profiles after the transition to H-mode and the build up of the pedestal density, similar to the density behaviour in JET reported in this work and in previous studies [40]. The investigation of the time scales of this transient density behaviour as a function of plasma parameters and size is certainly of interest for ITER (and DEMO) projections. In ITER, this hollow density transient phase should be at least beneficial in avoiding W accumulation in this initial phase. Later, during the current flat top phase of the ITER standard scenario, we expect the electron density profile to be moderately peaked in the confinement region [67–69], but flat in the innermost region close to the magnetic axis. In fact, in ITER no central bulk plasma particle source is present, and the Ware pinch is small, therefore no effect leading to density peaking is present close to the center. However, in ITER He ash will have a central particle source, provided by fusion reactions, which, at the same time, are a central sink for deuterons and tritons. This will generate central peaking of the He ash density profile, and the amount of peaking is predicted to depend on the He ash concentration, and therefore on the He pumping efficiency [54]. Consequently, density profiles of deuterium and tritium with a certain degree of hollowness in the region close to the magnetic axis can be expected in the presence of a flat electron density profile in that central region. The investigation of the impact of this interplay on the W behaviour, including the effect of the central peaking of He ash on the neoclassical W pinch by collisions between W and He in combination with the role of central heating produced by fusion reactions, should deserve some consideration. An additional element to be considered is that the central Mach number in ITER can be expected to be significantly smaller than in NBI heated plasmas in present devices due to the large plasma inertia and large heating power relative to the externally applied torque. This has at least the favorable consequence of producing a smaller rotational enhancement of W neoclassical transport with respect to present plasmas with strong NBI torque, and should therefore allow the turbulent transport component, also driven by central α heating, to compete more efficiently against the neoclassical pinch.

As a final remark, on the basis of the results of the present study on JET, it appears that accurate measurements of the main plasma density (and temperature) profiles close to the magnetic axis are an essential requirement. They play a critical role not only to perform a reliable validation of the theoretical models which predict W transport, but also for any comprehensive investigation of the W behaviour from the experimental standpoint, in order to relate the behaviour of W to that of the background plasma profiles.

Acknowledgments. The Authors are deeply grateful to E. Joffrin for having contributed to the coordination and the development of hybrid scenarios in JET with ILW and to the entire JET Team, in particular for the support in solving specific diagnostic related problems. This work was supported by EURATOM and carried out within the framework of the European Fusion Development Agreement. The views and opinions expressed herein do not necessarily reflect those of the European Commission.

Appendix: Transformation of the transport coefficients from LFS density to flux-surface averaged density

In the presence of a poloidally asymmetric density $n(r, \theta)$ of a particle species like W, the flux surface averaged particle flux Γ can be expressed as a function of the flux-surface averaged (FSA) density $n(r) = \langle n(r, \theta) \rangle$ or as a function of densities evaluated at specific locations or poloidal angles. A natural choice, for instance, is $n_0(r) = n(r, \theta = 0)$, evaluated at the LFS $\theta = 0$ location, which is adopted by codes like GKW and NEO. In this Appendix, we provide the equations to transform the corresponding transport coefficients from one description to the other. This is practical for many applications, in particular when the output of codes which can include 2D poloidal asymmetries has to be used inside usual 1D transport codes, which consider only 1D (or in any case FSA) quantities.

The FSA particle flux is expressed in the two forms

$$\Gamma = -D \frac{dn}{dr} + Vn,$$

and

$$\Gamma = -D_0 \frac{dn_0}{dr} + V_0 n_0.$$

and we state that these two forms are equivalent. Here, we shall make this equivalence explicit.

We note that the first expression for Γ involves the FSA density $n(r) = \langle n(r, \theta) \rangle$, and the corresponding transport coefficients D and V . In contrast, the second expression involves the LFS density $n_0 = n(r, \theta = 0)$ and the corresponding transport coefficients D_0 and V_0 .

We remind that in general

$$n(r, \theta) = n_0(r) \exp \left\{ -\frac{Ze\Phi(r, \theta)}{T(r)} + \frac{m\Omega^2(r)}{2T(r)} (R(r, \theta)^2 - R_0(r)^2) \right\} \quad (.1)$$

where Φ is the background electrostatic potential, defined in such a way that $\Phi(r, \theta = 0) = 0$, and $R_0(r)$ is the major radius of the location where n_0 is evaluated (usually LFS $\theta = 0$).

We introduce also the auxiliary (species dependent) normalized energy

$$E(r, \theta) = \frac{Ze\Phi(r, \theta)}{T(r)} - \frac{m\Omega^2(r)}{2T(r)} (R(r, \theta)^2 - R_0(r)^2) \quad (.2)$$

For clarity, with circular concentric flux surfaces, $R(r, \theta) = R_{\text{geo}} + r \cos \theta$ and $R_0(r) = R_{\text{geo}} + r$.

In general flux tube geometry, θ is a generalized poloidal angle, which describes the distance along the field line. Considering the right handed system of coordinates (r, θ, ϕ) , the flux surface average of the quantity $n(r, \theta)$ is given by

$$\langle f \rangle = \frac{1}{V'} \oint d\theta d\phi \sqrt{g} n(r, \theta),$$

where $g = (\nabla r \times \nabla \theta \cdot \nabla \phi)^{-2}$ is the determinant of the metric tensor, and $V' = dV/dr$, where $V(r)$ is the plasma volume up to the flux surface r .

Then, the following relationship holds,

$$\frac{d\langle n(r, \theta) \rangle}{dr} = \left\langle \frac{\partial n(r, \theta)}{\partial r} \right\rangle + n_0(r) \mathcal{G}_r, \quad (.3)$$

where we have defined

$$\mathcal{G}_r = \left[-\frac{1}{V'} \frac{d^2 V}{dr^2} \langle n(r, \theta) \rangle + \frac{1}{V'} \oint d\theta d\phi n(r, \theta) \frac{\partial \sqrt{g}}{\partial r} \right] n_0(r)^{-1}$$

that is

$$\mathcal{G}_r = -\frac{1}{V'} \frac{d^2 V}{dr^2} \langle \exp \{-E(r, \theta)\} \rangle + \left\langle \exp \{-E(r, \theta)\} \frac{\partial \log(\sqrt{g})}{\partial r} \right\rangle$$

Partial derivatives versus the minor radius r are intended to be performed at constant θ . We note that $\mathcal{G}_r = 0$ with a Hamada coordinate system (as used in GKW).

In order to derive the relationship between the two pairs (D, V) and (D_0, V_0) , we proceed by expressing the FSA density $n(r)$ and its radial derivative $dn(r)/d(r)$ in terms of $n_0(r)$ and $dn_0(r)/d(r)$. The relationship between $n(r)$ and $n_0(r)$ is straightforward

$$n(r) = n_0(r) \left\langle \exp \left\{ -\frac{Ze\Phi(r, \theta)}{T(r)} + \frac{m\Omega^2(r)}{2T(r)} (R(r, \theta)^2 - R_0(r)^2) \right\} \right\rangle$$

In order to express $dn(r)/d(r)$ in terms of $n_0(r)$ and $dn_0(r)/d(r)$, we proceed with the computation of $\partial n(r, \theta)/\partial r$. and by taking the FSA and recalling Eq. .3, we find,

$$\begin{aligned} \frac{dn(r)}{dr} &= \langle \exp \{-E(r, \theta)\} \rangle \frac{dn_0(r)}{dr} + \\ &+ n_0(r) \left\{ - \left\langle \exp \{-E(r, \theta)\} \frac{Ze}{T(r)} \frac{\partial \Phi(r, \theta)}{\partial r} \right\rangle \right. \\ &+ \left\langle \exp \{-E(r, \theta)\} (R(r, \theta)^2 - R_0(r)^2) \right\rangle \frac{m\Omega}{T(r)} \frac{d\Omega(r)}{dr} \\ &+ \left\langle \exp \{-E(r, \theta)\} \frac{\partial}{\partial r} (R(r, \theta)^2 - R_0(r)^2) \right\rangle \frac{m\Omega^2}{2T(r)} \\ &+ \left\langle \exp \{-E(r, \theta)\} \frac{Ze}{T(r)} \Phi(r, \theta) \right\rangle \frac{1}{T(r)} \frac{dT(r)}{dr} \\ &\left. - \left\langle \exp \{-E(r, \theta)\} (R(r, \theta)^2 - R_0(r)^2) \right\rangle \frac{m\Omega^2}{2T(r)} \frac{1}{T(r)} \frac{dT(r)}{dr} \right\} + n_0(r) \mathcal{G}_r. \end{aligned}$$

At this point, we replace the expressions of $dn(r)/dr$ and $n(r)$ in the expression for Γ and we obtain

$$\begin{aligned}
\Gamma = & -D \langle \exp \{-E(r, \theta)\} \rangle \frac{dn_0(r)}{dr} + \\
& -D n_0(r) \left\{ - \left\langle \exp \{-E(r, \theta)\} \frac{Ze}{T(r)} \frac{\partial \Phi(r, \theta)}{\partial r} \right\rangle \right. \\
& + \left\langle \exp \{-E(r, \theta)\} (R(r, \theta)^2 - R_0(r)^2) \right\rangle \frac{m\Omega}{T(r)} \frac{d\Omega(r)}{dr} \\
& + \left\langle \exp \{-E(r, \theta)\} \frac{\partial}{\partial r} (R(r, \theta)^2 - R_0(r)^2) \right\rangle \frac{m\Omega^2}{2T(r)} \\
& + \left\langle \exp \{-E(r, \theta)\} \frac{Ze}{T(r)} \Phi(r, \theta) \right\rangle \frac{1}{T(r)} \frac{dT(r)}{dr} \\
& - \left. \left\langle \exp \{-E(r, \theta)\} (R(r, \theta)^2 - R_0(r)^2) \right\rangle \frac{m\Omega^2}{2T(r)} \frac{1}{T(r)} \frac{dT(r)}{dr} + \mathcal{G}_r \right\} \\
& + V n_0(r) \langle \exp \{-E(r, \theta)\} \rangle
\end{aligned}$$

Finally, we compare with equation

$$\Gamma = -D_0 \frac{dn_0}{dr} + V_0 n_0,$$

and we easily derive the sought relationships:

$$D = D_0 \langle \exp \{-E(r, \theta)\} \rangle^{-1} = D_0 \frac{n_0}{n},$$

$$\begin{aligned}
V = & V_0 \langle \exp \{-E(r, \theta)\} \rangle^{-1} + D_0 \left\{ - \left\langle \exp \{-E(r, \theta)\} \frac{Ze}{T(r)} \frac{\partial \Phi(r, \theta)}{\partial r} \right\rangle \right. \\
& + \left\langle \exp \{-E(r, \theta)\} (R(r, \theta)^2 - R_0(r)^2) \right\rangle \frac{m\Omega}{T(r)} \frac{d\Omega(r)}{dr} \\
& + \left\langle \exp \{-E(r, \theta)\} \frac{\partial}{\partial r} (R(r, \theta)^2 - R_0(r)^2) \right\rangle \frac{m\Omega^2}{2T(r)} \\
& + \left\langle \exp \{-E(r, \theta)\} \frac{Ze}{T(r)} \Phi(r, \theta) \right\rangle \frac{1}{T(r)} \frac{dT(r)}{dr} \\
& - \left. \left\langle \exp \{-E(r, \theta)\} (R(r, \theta)^2 - R_0(r)^2) \right\rangle \frac{m\Omega^2}{2T(r)} \frac{1}{T(r)} \frac{dT(r)}{dr} + \mathcal{G}_r \right\} \\
& \cdot \langle \exp \{-E(r, \theta)\} \rangle^{-2}
\end{aligned} \tag{.4}$$

For simplicity, we define the following conversion factor for the convection,

$$\begin{aligned}
\mathcal{V} = a & \left\{ - \left\langle \exp \{-E(r, \theta)\} \frac{Ze}{T(r)} \frac{\partial \Phi(r, \theta)}{\partial r} \right\rangle \right. \\
& + \left\langle \exp \{-E(r, \theta)\} \left(R(r, \theta)^2 - R_0(r)^2 \right) \right\rangle \frac{m\Omega}{T(r)} \frac{d\Omega(r)}{dr} \\
& + \left\langle \exp \{-E(r, \theta)\} \frac{\partial}{\partial r} \left(R(r, \theta)^2 - R_0(r)^2 \right) \right\rangle \frac{m\Omega^2}{2T(r)} \\
& + \left\langle \exp \{-E(r, \theta)\} \frac{Ze}{T(r)} \Phi(r, \theta) \right\rangle \frac{1}{T(r)} \frac{dT(r)}{dr} \\
& - \left\langle \exp \{-E(r, \theta)\} \left(R(r, \theta)^2 - R_0(r)^2 \right) \right\rangle \frac{m\Omega^2}{2T(r)} \frac{1}{T(r)} \frac{dT(r)}{dr} + \mathcal{G}_r \left. \right\} \\
& \cdot \langle \exp \{-E(r, \theta)\} \rangle^{-1}, \tag{.5}
\end{aligned}$$

by which the transformation from the pair (D_0, V_0) into the pair (D, V) simply reads

$$D = \langle \exp \{-E(r, \theta)\} \rangle^{-1} D_0 = \frac{n_0}{n} D_0, \tag{.6}$$

$$aV = \langle \exp \{-E(r, \theta)\} \rangle^{-1} (aV_0 + D_0 \mathcal{V}). \tag{.7}$$

Here we have introduced an arbitrary normalizing length a (usually the geometrical major radius R_{geo} in GKW and the minor radius a in NEO).

The quantity \mathcal{V} can be directly computed inside codes which treat poloidal aysmmetries (like GKW and NEO).

Finally, we notice that the convection conversion factor \mathcal{V} has been defined in such a way that

$$\frac{aV}{D} = \frac{aV_0}{D_0} + \mathcal{V}, \tag{.8}$$

which can be also regarded as a direct consequence of the following relationship

$$\frac{a}{n} \frac{dn}{dr} = \frac{a}{n_0} \frac{dn_0}{dr} + \mathcal{V}.$$

REFERENCES

- [1]. Matthews G.F. et al 2011 *Physica Scripta* 2011 014001.
- [2]. Neu R. et al 2013 *Physics of Plasmas* **20** 056111.
- [3]. Joffrin E. et al 2014 *Nuclear Fusion* **54** 013011.
- [4]. Beurskens M.N.A., Schweinzer J. et al 2013 *Plasma Physics and Controlled Fusion* **55** 124043.
- [5]. Pütterich T., Dux R., Neu R., et al 2013 *Plasma Physics and Controlled Fusion* **55** 124036.
- [6]. Sips A.C.C. et al 2002 *Plasma Physics and Controlled Fusion* **44** B69.
- [7]. Luce T. et al 2003 *Nuclear Fusion* **43** 321.
- [8]. Joffrin E. et al 2005 *Nuclear Fusion* **45** 626.
- [9]. Dux R., Neu R., Peeters A.G., Pereverzev G., Mück A., Rytter F., Stober J., *Plasma Physics and Controlled Fusion* **45**, 1815 (2003).
- [10]. Neu R. et al 2003 *Journal of Nuclear Materials* **313** 116.
- [11]. Carraro L. et al 2004 *Plasma Physics and Controlled Fusion* **46** 389.
- [12]. Puiatti M.E., Valisa M., Angioni C., Garzotti L., Mantica P., Mattioli M., Carraro L., Coffey I., Sozzi C. 2006 *Phys. Plasmas* **13** 042501.
- [13]. Rice J.E. et al 2007 *Fusion Science and Technology* **51** 357.
- [14]. Guirlet R. et al 2009 *Nuclear Fusion* **49** 055007.
- [15]. Villegas D., Guirlet R., Bourdelle C., Hoang G.T., Garbet X. and Sabot R. 2010 *Physical Review Letters* 105 035002.
- [16]. Valisa M. et al 2011 *Nuclear Fusion* **51** 033002.
- [17]. Sertoli M. et al 2011 *Plasma Physics and Controlled Fusion* **53** 035024.
- [18]. Howard N.T. et al 2012 *Nuclear Fusion* **52** 063002.
- [19]. Howard N.T. et al 2012 *Physics of Plasmas* **19** 056110.
- [20]. Reinke M.L. et al 2012 *Plasma Physics and Controlled Fusion* **54** 045004.
- [21]. Angioni C. and Peeters A.G. 2006 *Physical Review Letters* **96** 095003.
- [22]. Dubuit N., Garbet X., Parisot T., Guirlet R., and Bourdelle C. 2007 *Physics of Plasmas* **14** 042301.
- [23]. Angioni C. et al 2007 *Physics of Plasmas* **14** 055905.
- [24]. Nordnam H et al 2008 *Physics of Plasmas* **15** 042316.
- [25]. Camenen Y., Peeters A.G., Angioni C. et al 2009 *Physics of Plasmas* **16** 012503.
- [26]. Fülöp T., Braun S., and Pusztai 2010 *Physics of Plasmas* **17** 062501.
- [27]. Fülöp T. and Moradi S. 2011 *Physics of Plasmas* **18** 030703.
- [28]. Skyman A. 2012 *Physics of Plasmas* **19** 032313.
- [29]. Mollen A. et al 2012 *Physics of Plasmas* **19** 052307.
- [30]. Angioni C. et al 2012 *Physics of Plasmas* **19** 122311.
- [31]. Pütterich T. et al 2012 Tungsten Screening and Impurity Control in JET, IAEA Fusion Energy Conf., San Diego, EX/P3–15.
- [32]. Lauro Taroni L. et al 1994 Proc. 21st EPS Conf. Controlled Fusion and Plasma Physics, Montpellier, France, Vol. 1, p. 102 (1994).

- [33]. Whiteford A.D. et al 2004 31st Conf. on Controlled Fusion and Plasma Physics (London, 2004) vol 28G P1.159; Whiteford A.D. 2004 On the spectral emission of impurity species for diagnostic application to magnetically confined fusion plasmas PhD Thesis University of Strathclyde, Glasgow (UK).
- [34]. Koskela T, private communication
- [35]. Belli E. and Candy J. 2008 Plasma Physics and Controlled Fusion **50** 095010.
- [36]. Belli E. and Candy J. 2012 Plasma Physics and Controlled Fusion **54** 015015.
- [37]. Peeters A.G. et al 2009 Computer Physics Communications **180** 2650.
- [38]. Casson F. J. et al 2010 Physics of Plasmas **17** 102305.
- [39]. Alper B. et al 1997 Review of Scientific Instruments **68** 778.
- [40]. Loarte A. et al 2013 Nuclear Fusion **53** 083031.
- [41]. Wong S.K. 1987 Physics of Fluids **30** 818.
- [42]. Romanelli M., Ottaviani M. 1998 Plasma Physics and Controlled Fusion **40** 1757.
- [43]. Fülöp T. and Helander P. 1999 Physics of Plasmas **6** 3066.
- [44]. Angioni C, Helander P. 2014 Plasma Physics and Controlled Fusion submitted.
- [45]. Belli E., Candy J., Angioni C. 2014 Plasma Physics and Controlled Fusion submitted.
- [46]. Angioni C. et al 2011 Nuclear Fusion **51** 023006.
- [47]. Cenacchi G., Taroni A., 1988, Rapporto ENEA RT/TIB (88)5.
- [48]. Casson F.J. et al 2013 Nuclear Fusion **53** 063026.
- [49]. Lao L.L. et al 1985 Nuclear Fusion **25** 1421.
- [50]. O'Brien D. P. et al 1992 Nuclear Fusion **32** 1351.
- [51]. Brix M., Hawkes N. C. et al 2008 Review of Scientific Instruments **79** 10F325.
- [52]. Hinton F.L. and Wong S.K. 1985 Physics of Fluids **28** 3082.
- [53]. Wesson J.A. 1997 Nuclear Fusion **37** 577.
- [54]. Angioni C., Peeters A.G., Pereverzev G.V., Bottino A., Candy J., Dux R., Fable E., Hein T. and Waltz R.E. 2009 Nuclear Fusion **49** 055013.
- [55]. Summers H.P. et al 2002 Plasma Physics and Controlled Fusion **44** B323 (<http://www.adas.ac.uk/>).
- [56]. Huber A. et al 2007 Fusion Engineering and Design **82** 1327.
- [57]. Ingesson L. C., Chen H., Helander P., and Mantsinen M. J. 2000 Plasma Physics and Controlled Fusion **42** 161.
- [58]. Reinke M. L. et al 2013 Physics of Plasmas **20** 056109.
- [59]. Odstrcil M., Mlynar J., Odstrcil T., Alper B., Murari A. 2012 Nuclear Instruments & Methods in Physics Research Section A **686** 9 156.
- [60]. Helander P. 1998 Physics of Plasmas **5** 3999.
- [61]. Reinke M.L. et al 2013 Nuclear Fusion **53** 043006.
- [62]. Reinke M.L. et al 2012 Review of Scientific Instruments **83** 113504.
- [63]. Hirshman S.P. and Sigmar D.J. 1981 Nuclear Fusion **21** 1079.
- [64]. Mantica P. et al 2013 40th European Physical Society Conference on Plasma Physics, Helsinki

2013, P4.141 (<http://ocs.ciemat.es/EPS2013ABS/pdf/P4.141.pdf>).

- [65]. Angioni C., Peeters A. G., Garbet X. et al 2004 Nuclear Fusion **44** 827.
 [66]. McDermott R.M. et al 2011 Plasma Physics and Controlled Fusion **53** 035007.
 [67]. Pereverzev G.V., Angioni C., Peeters A.G. and Zolotukhin O.V. 2005 Nuclear Fusion **45** 221.
 [68]. Angioni C., Weisen H., Kardaun O.J.W.F. et al. 2007 Nuclear Fusion **47** 1326.
 [69]. Angioni C., Candy J., Fable E., Maslov M., Waltz R.E., Weisen H. 2009 Physics of Plasmas **16** 060702.
 [70]. Bilato R., Maj O. and Angioni C. 2014 Nuclear Fusion submitted
 [71]. Houlberg W.A., Shaing K.C., Hirshman S.P., Zarnstorff M.C. 1997 Physics of Plasmas **4** 3230.
 [72]. Peeters A.G. 2000 Physics of Plasmas **7** 268.

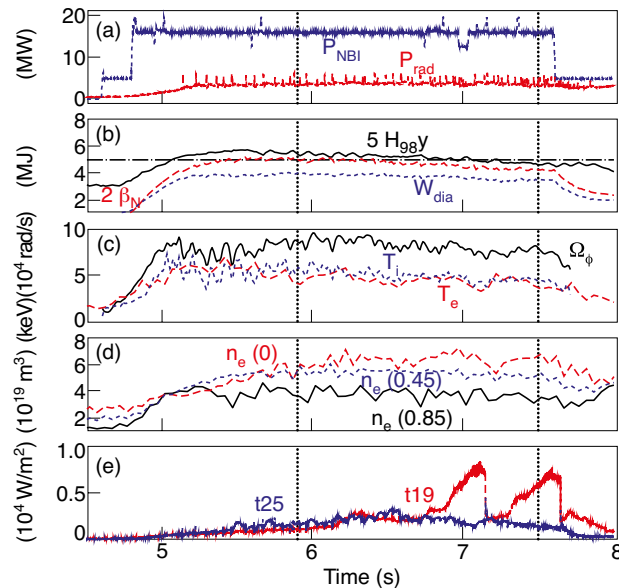


Figure 1: Time traces of (a) the NBI and the radiated power. (b) the total stored energy W_{dia} in MJ, the normalized pressure parameter β_N (times 2), and the H98y factor (times 5). (c) the central electron temperature, as well as ion (carbon) temperature and toroidal rotation, (d) the central, intermediate ($r/a = 0.45$) and peripheral (pedestal top $r/a = 0.85$) density, (e) the central and peripheral (chord tangent to magnetic surface $r/a = 0.4$) lines of sight of the SXR emission, during the high power phase of JET-ILW hybrid scenario Pulse No: 82722. Vertical dotted lines mark the time slices at which specific analysis and theory-based modelling have been performed.

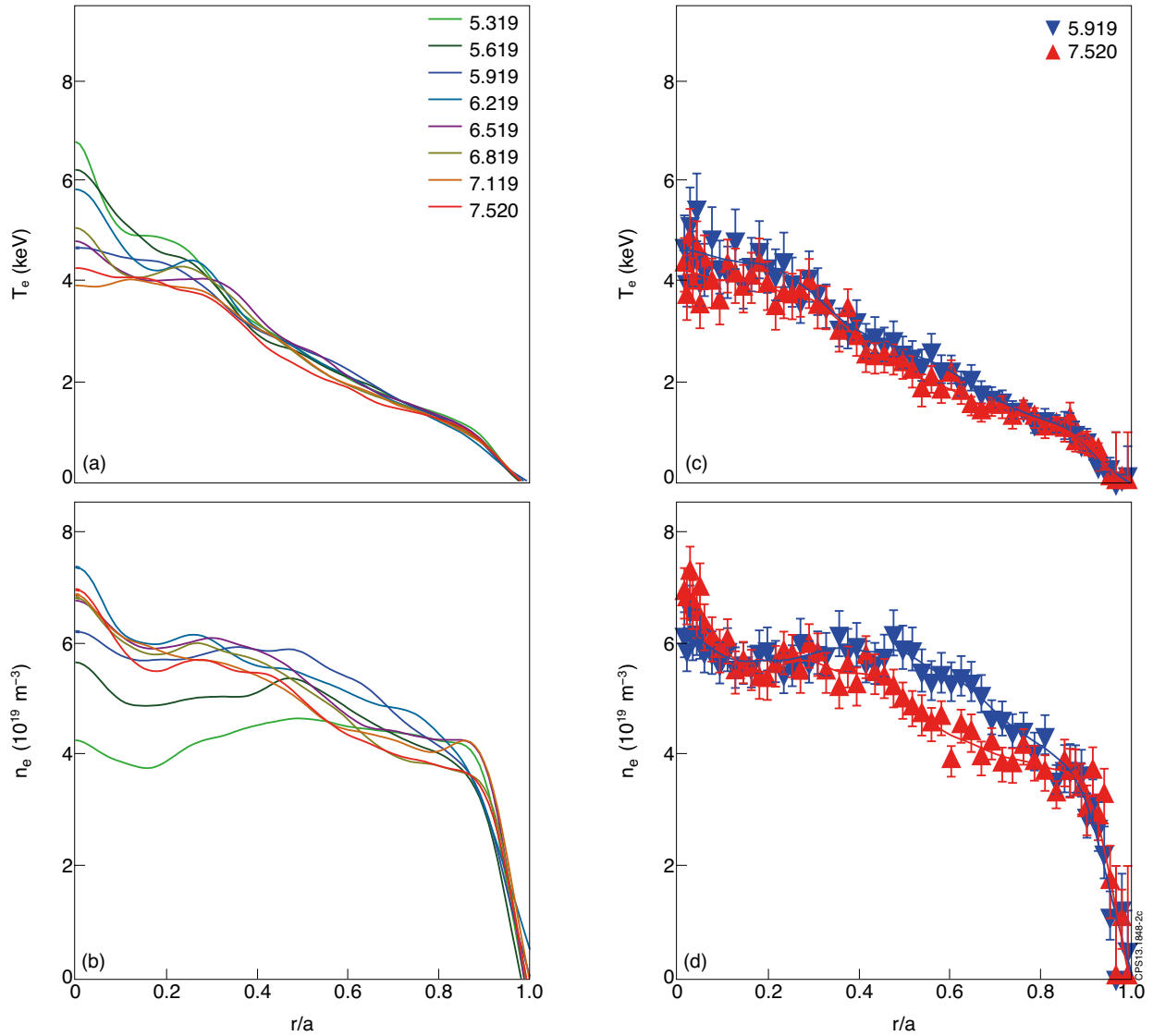


Figure 2: Selection of electron temperature (a) and density (b) profiles obtained by cubic spline fits of the JET HRTS diagnostic measurements, which illustrates the time evolution during the high power phase (after the NBI heating is switched on and H-mode is accessed) of JET-ILW hybrid scenario Pulse No: 82722. In the legend the corresponding times are quoted in s and curves in bold identify time slices at which the specific analysis, as well as the theoretical calculations, have been performed. The HRTS raw data of electron temperature and density at these two time slices (in s in the legend) are plotted in symbols with error bars in (c) and (d) respectively, together with the corresponding cubic spline fits.

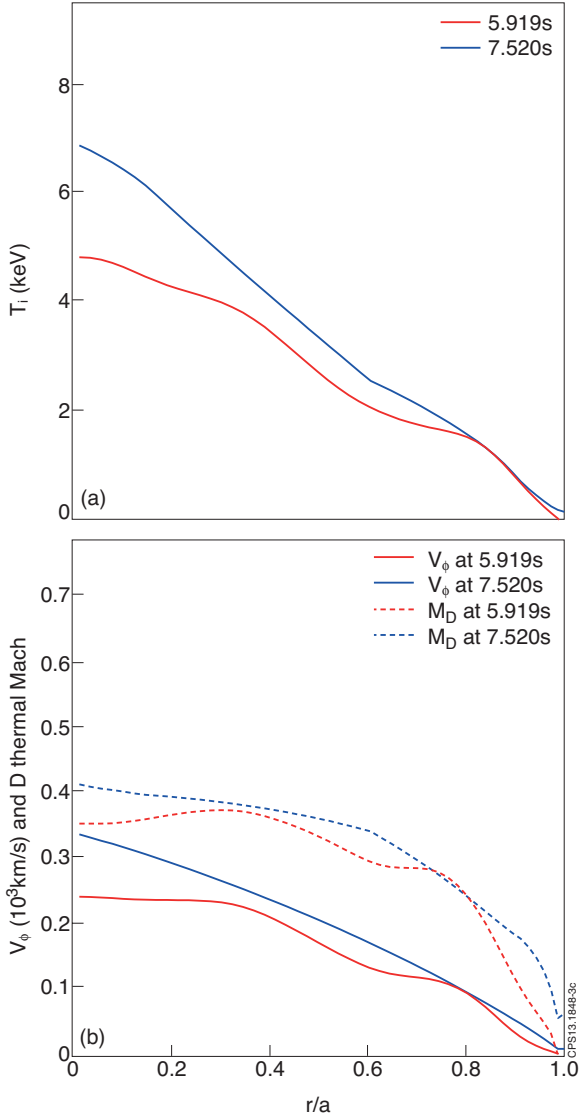


Figure 3: Profiles of ion temperature (a) and toroidal rotation (solid) and Mach number (dashed), normalized to D thermal velocity, (b) at the two times of the analysis, as obtained by JETTO interpolation of the raw data and used as inputs of the NEO and GKW codes.

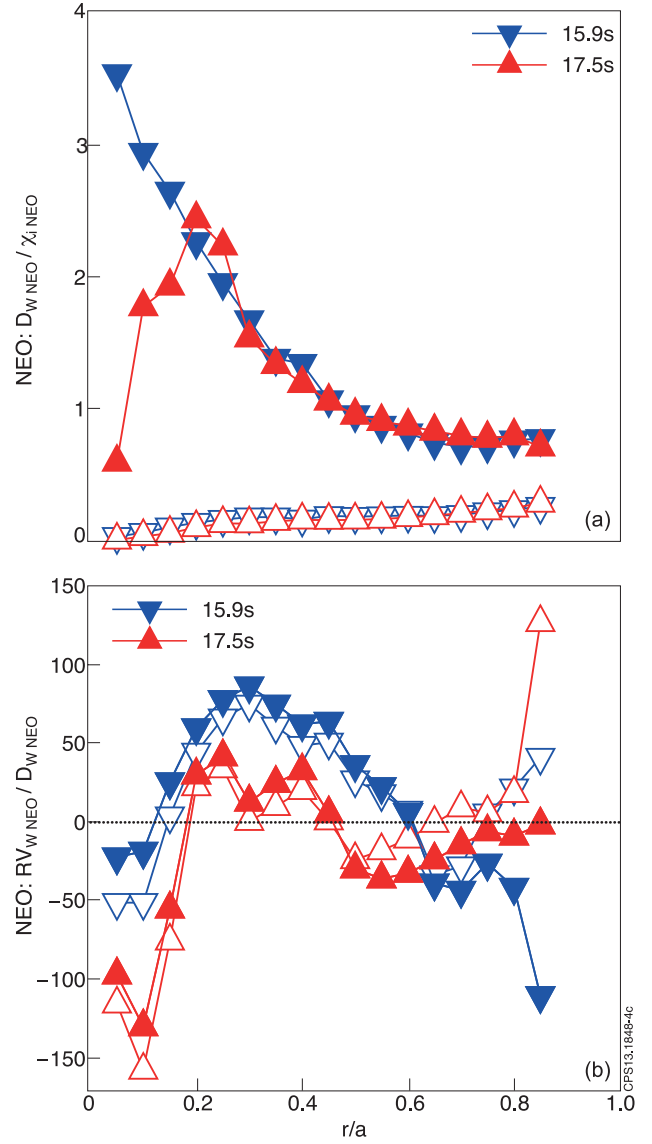


Figure 4: Profiles of the neoclassical W diffusion to ion heat conductivity ratio $D_{W\text{NEO}}/\chi_{i\text{NEO}}$ (a) and the neoclassical normalized W convection to diffusion ratio $RV_{W\text{NEO}}/D_{W\text{NEO}}$ (b) computed by NEO, with (full symbols) and without (open symbols) the inclusion of rotational (centrifugal) effects, at the two time slices 5.9s (triangles pointing down) and 7.5s (triangles pointing up).

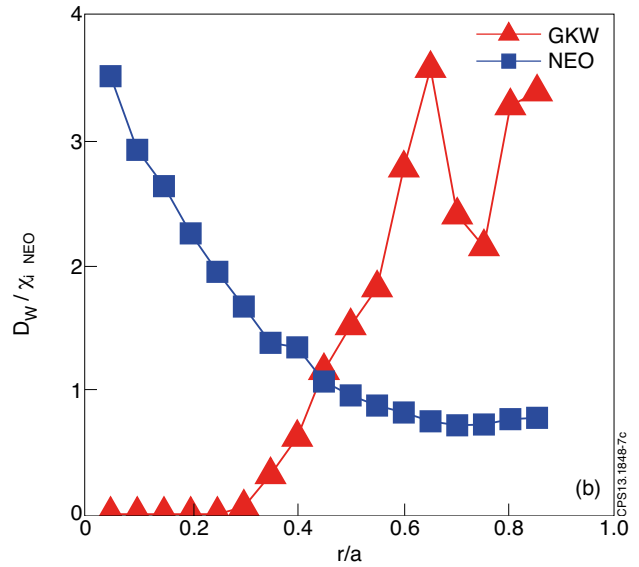
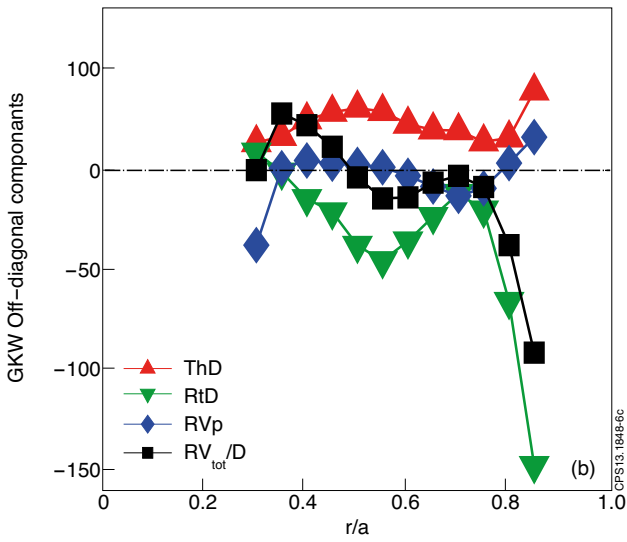
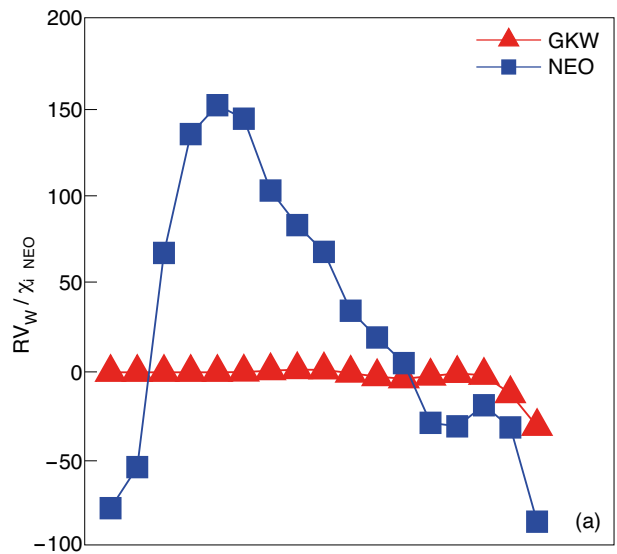
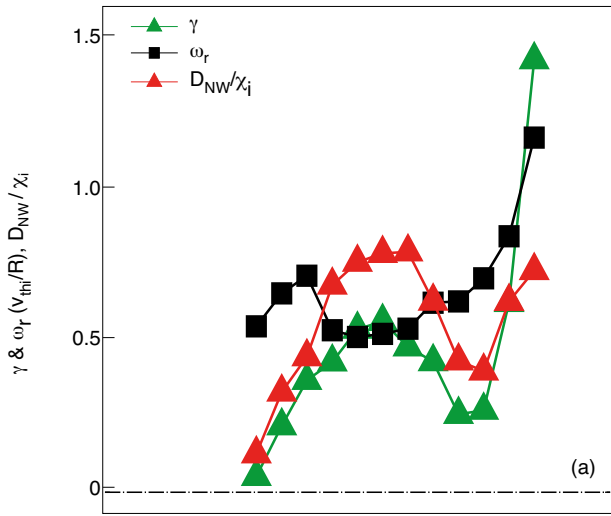


Figure 5: Growth rate and real frequency (a) as well as W transport coefficients (b) obtained with linear gyrokinetic calculations with GKW for the time slice 5.9s.

Figure 6: Growth rate and real frequency (a) as well as W transport coefficients (b) obtained with linear gyrokinetic calculations with GKW for the time slice 7.5s.

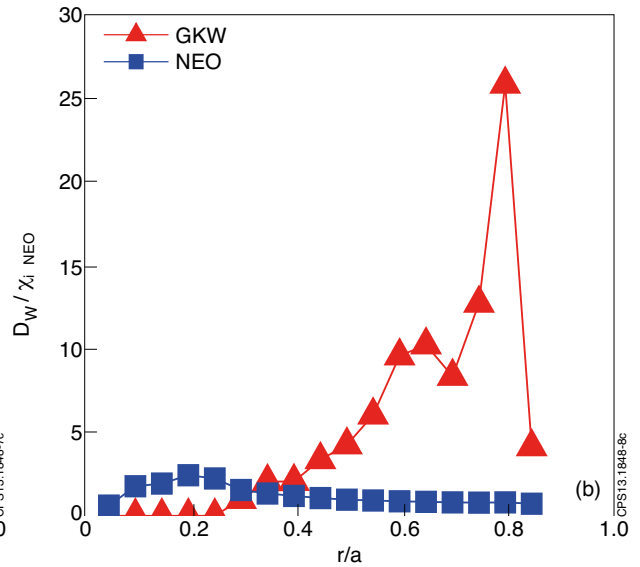
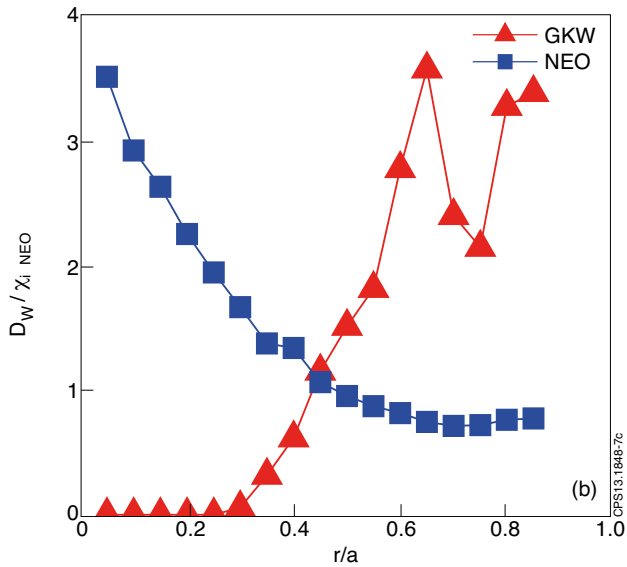
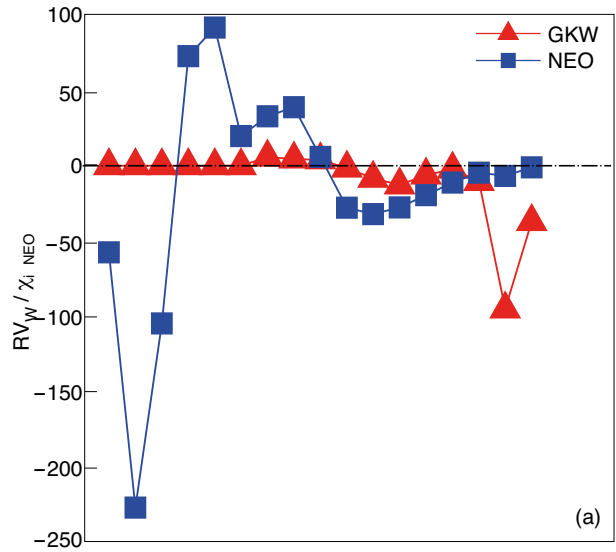
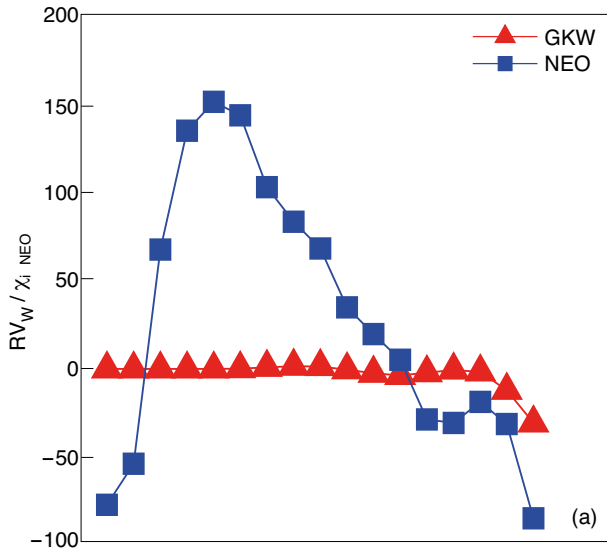


Figure 7: Neoclassical (NEO) and turbulent (GKW) convective (a) and diffusive (b) contributions normalized to the neoclassical ion heat conductivity as they appear in the numerator (a) and denominator (b) of Eq. (3), for the time slice 5.9s.

Figure 8: Neoclassical (NEO) and turbulent (GKW) convective (a) and diffusive (b) contributions normalized to the neoclassical ion heat conductivity as they appear in the numerator (a) and denominator (b) of Eq. (3), for the time slice 7.5s.

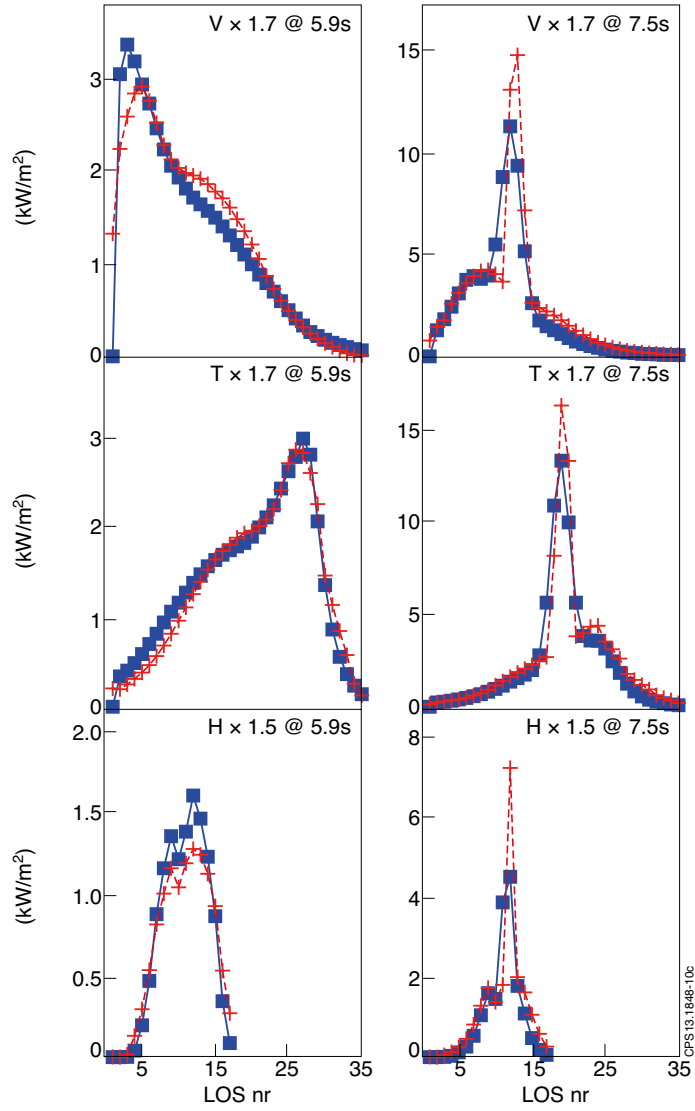


Figure 9: Radial profiles of the logarithmic gradient of the LFS density predicted by the combined neoclassical and turbulent transport contributions as computed with NEO and GKW respectively (a), and the corresponding integrated LFS density profiles at the two time slices 5.9s (squares) and 7.5s (triangles pointing up). Dash-dotted lines show the result in the W trace limit for the strong accumulation phase.

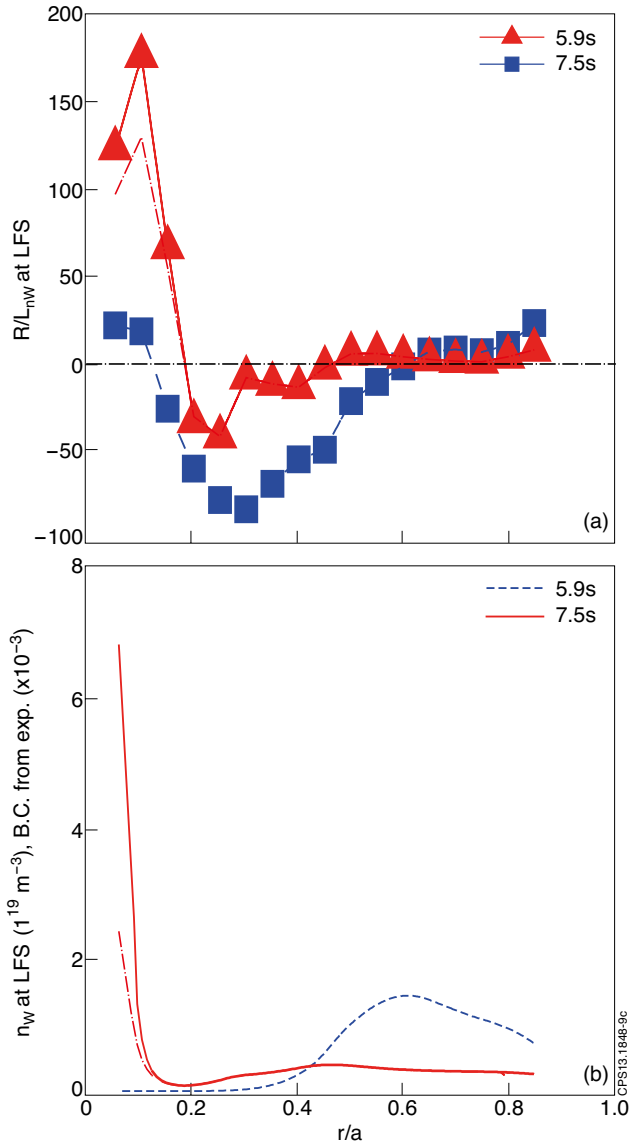


Figure 10: Comparison between measured signals of line integrated SXR emission from lines of sight (LOS) of JET SXR cameras, with appropriate calibration factors (squares) and JETTO/SANCO and UTC modelling results ('+' crosses), at 5.9s (left) and 7.5s (right).

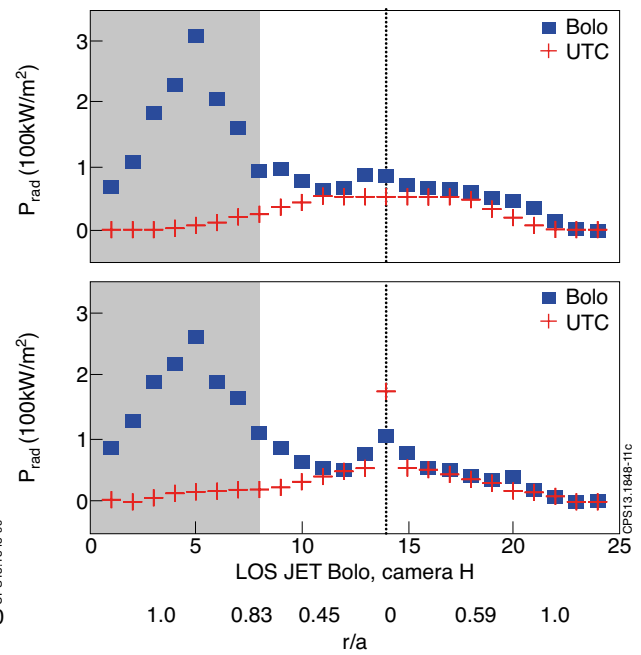


Figure 11: Comparison between the line integrated radiated power from the lines of sight (LOS) of the horizontal camera of the JET bolometric diagnostic (squares) and the results of the JETTO/SANCO and UTC simulations ('+' crosses). The uncertainty on the bolometric measurements is estimated to be 3%, due to typical noise level in the raw data. The corresponding values of r/a of the flux surfaces tangent to some of the lines of sight are also quoted for reference. The LOS going through the magnetic axis is identified with a vertical dotted line, and the shaded area identifies the LOS from 1 to 8 which look at the divertor region and therefore are beyond the spatial domain of interest covered by the JETTO/SANCO simulations.

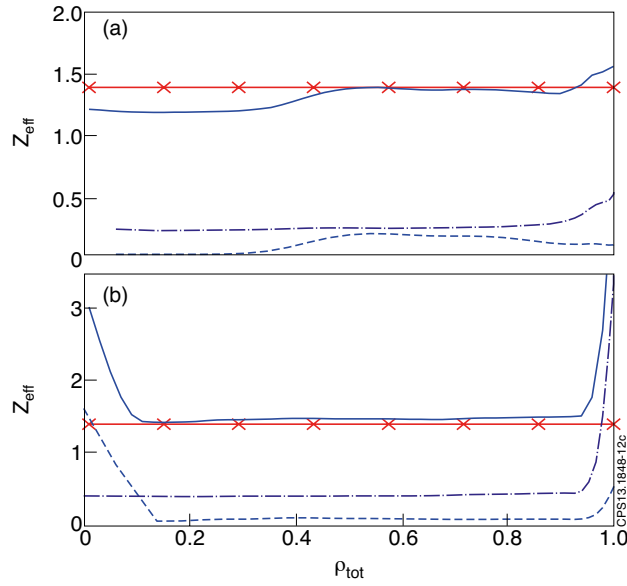


Figure 12: Profiles of the total effective charge Z_{eff} (solid) and relative contributions from W $\Delta Z_{\text{eff}W}$ (dashed) and from Be $\Delta Z_{\text{eff}Be}$ (dash-dotted) as obtained by the JETTO/SANCO analysis and compared with the line averaged values from visible spectroscopy (solid with crosses), at 5.9s (a) and 7.5s (b).

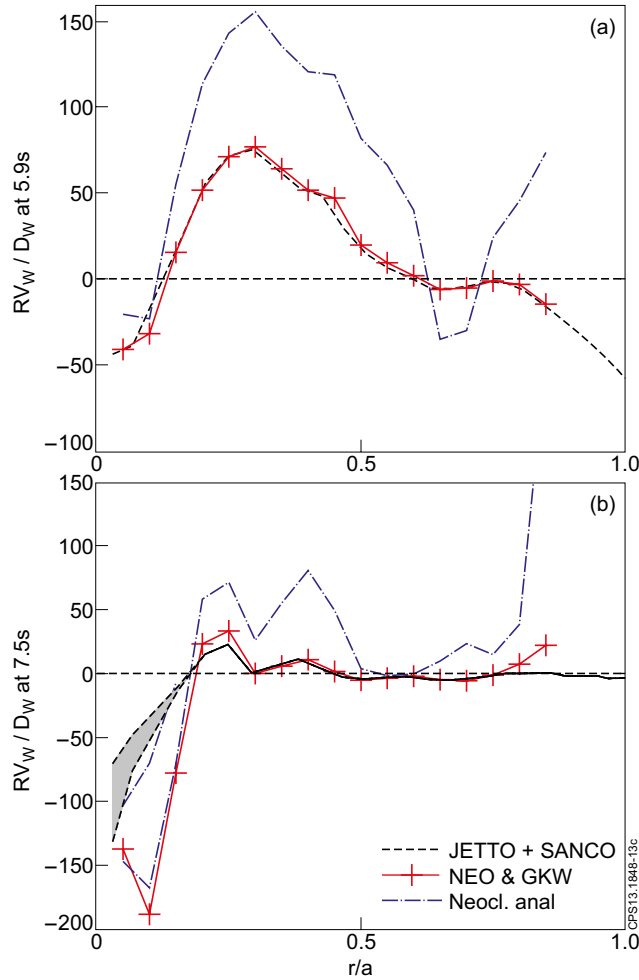


Figure 13: Radial profiles of the FSA convection to diffusion ratio obtained by the JETTO/SANCO interpretive modelling (dashed lines), by the NEO and GWK predictions (solid lines) and by an analytic neoclassical transport estimate ($Z(R/L_n - 0.5R/L_{Ti})$) (dash-dotted lines) at 5.9s (a) and 7.5s (b). The shaded area in (b) shows the uncertainty over which equally good fits of the measurements are obtained with the JETTO/SANCO analysis.

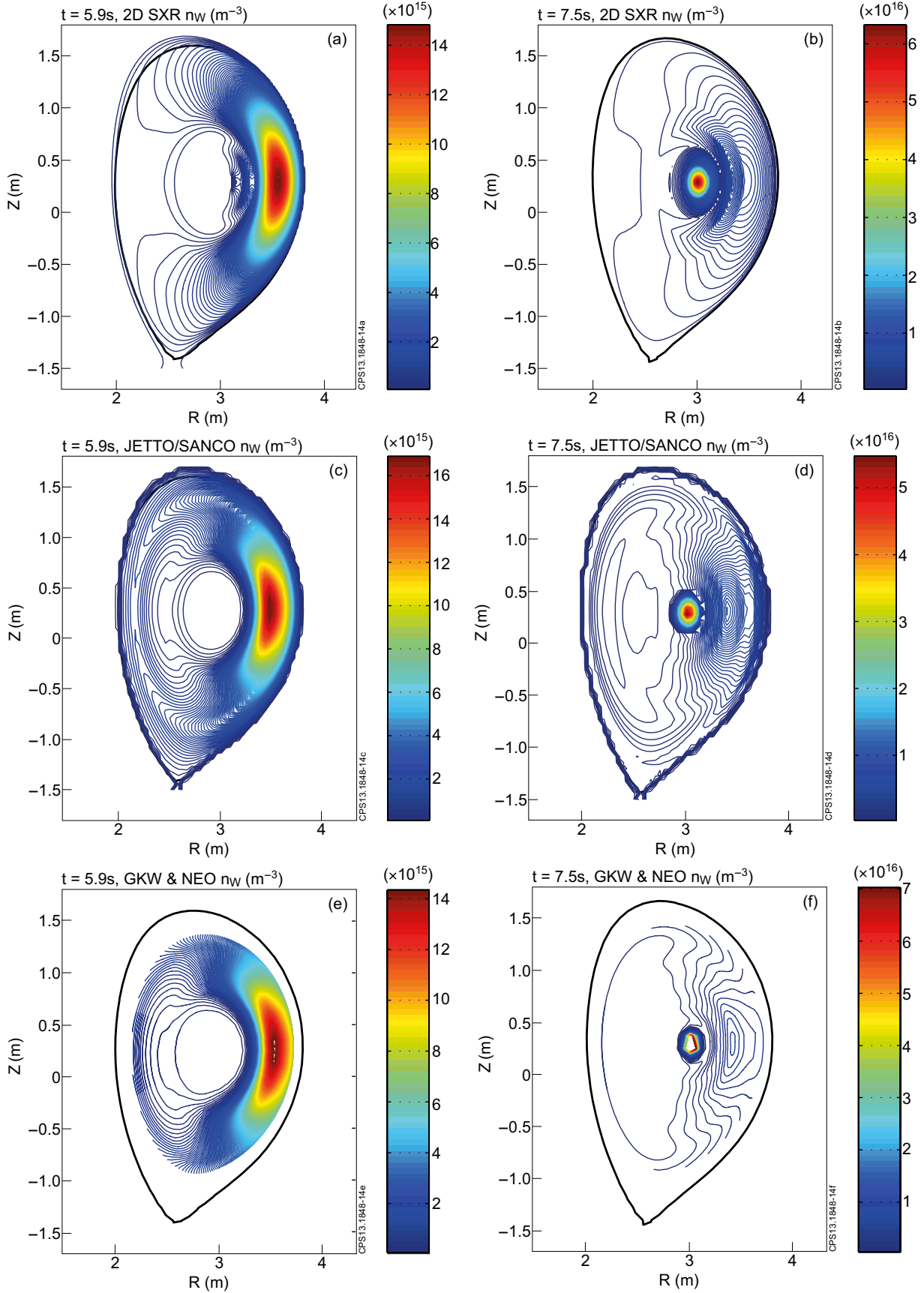


Figure 14: Contour lines of W density on the poloidal cross section at 5.9s (a,c,e) and 7.5s (b,d,f), as obtained from the SXR 2D W density diagnostic (a,b), by the JETTO/SANCO analysis post-processed with UTC and SXRPHY, and as predicted by the combined calculations of GKW and NEO (e,f).

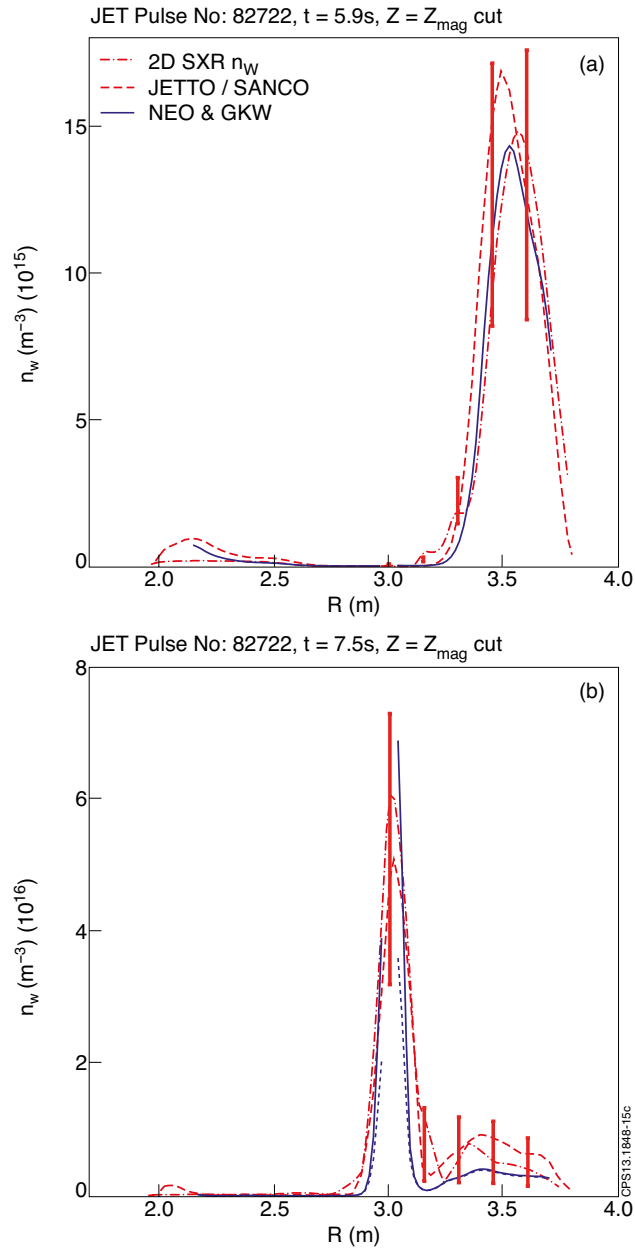


Figure 15: W density as a function of major radius in a horizontal cut at the magnetic axis height at 5.9s (a) and 7.5 s (b). Dashed lines show the results of the JETTO/SANCO interpretive analysis, dash-dotted lines the results of the 2D SXR W density diagnostic, and solid lines show the results of the combined GWK and NEO calculations. The dotted curve in (b) shows the predictions obtained in the W trace limit. The magnetic axis is located at 3.01m.

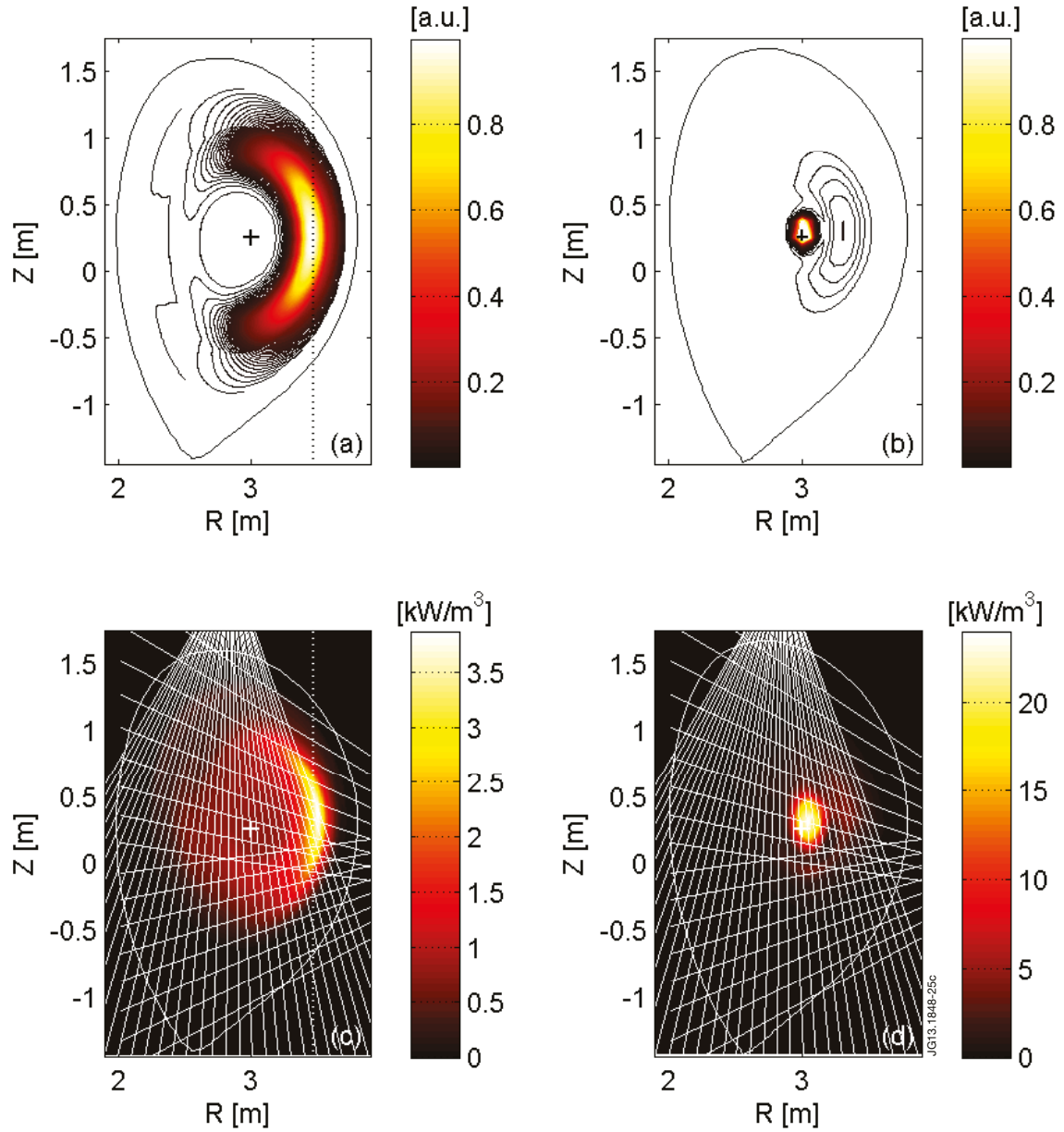


Figure 16: 2D distribution over the poloidal cross-section of the predicted SXR emission produced by W only at 5.9s (a) and 7.5s (b), and, for comparison, the SXR tomography at 5.9s (c) and 7.5s (d) of the integral SXR emissivity (including Bremsstrahlung from the bulk plasma). Dotted lines show the LOS of the three SXR cameras.

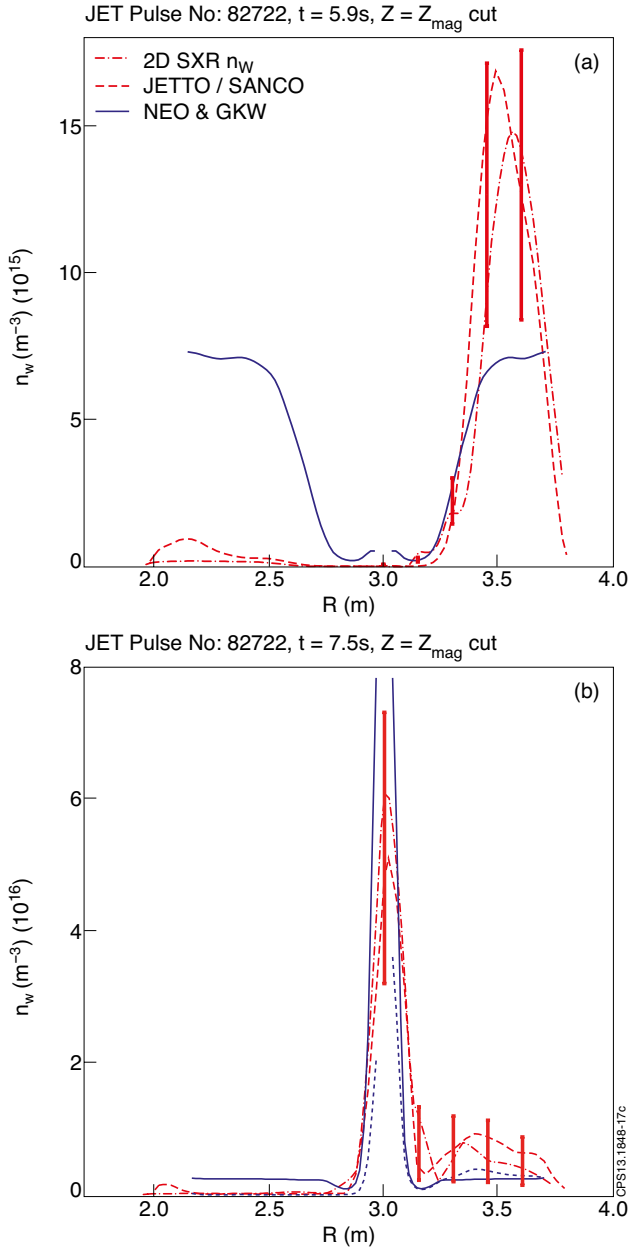


Figure 17: W density as a function of major radius in a horizontal cut at the magnetic axis height at 5.9s (a) and 7.5s (b). The experimental curves (same curves as in Fig.15) are compared with the theoretical results obtained without the inclusion of centrifugal effects.

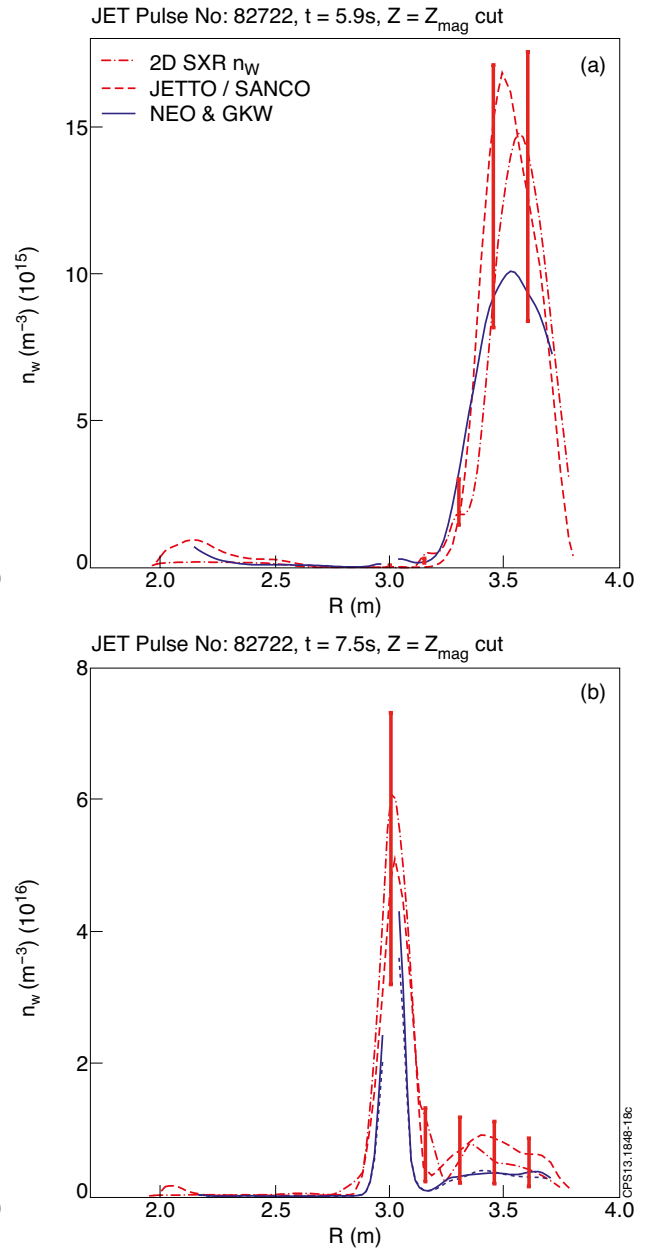


Figure 18: W density as a function of major radius in a horizontal cut at the magnetic axis height at 5.9s (a) and 7.5s (b). The experimental curves (same curves as in Fig.15) are compared with the theoretical results obtained without the inclusion the centrifugal effects, but the resulting density is interpreted as a flux surface averaged density and remapped on the poloidal cross section considering the poloidal asymmetries produced by centrifugal effects.

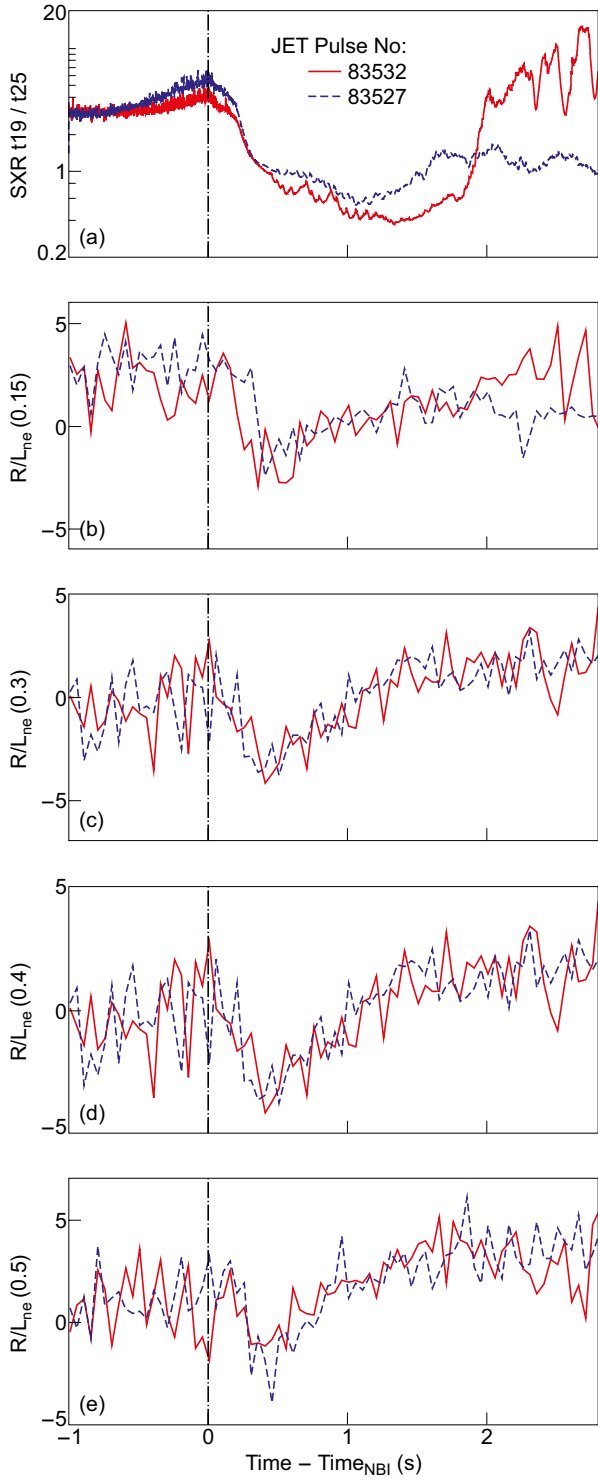


Figure 19: Comparison of the time evolution of the ratio of a central to a peripheral LOS of the SXR camera (t_{19}/t_{25}) (a), and of the normalized logarithmic electron density gradient at different radial positions (b-e) between the two Pulse No's: 83532 and 83527. In order to enable a direct comparison, on the x-axis, time is counted from the time of the NBI switch on ($time_{NBI}$), which in Pulse No: 83527 takes place 0.5s earlier than in Pulse No: 83532.

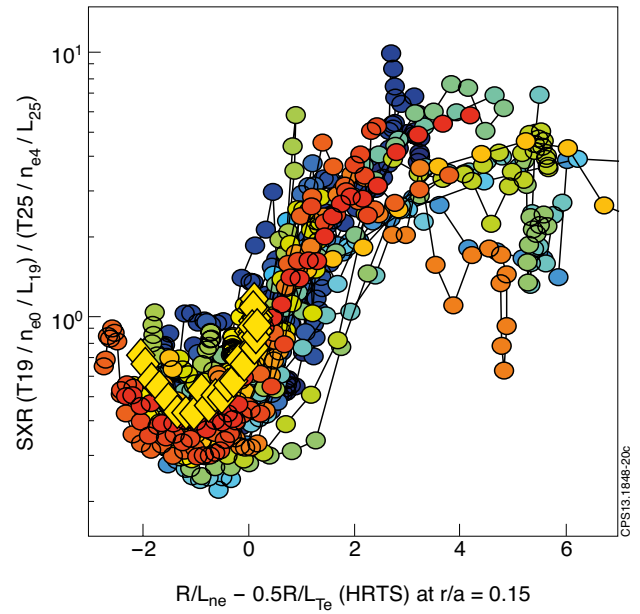


Figure 20: Proxy of W LFS peaking vs proxy of neoclassical pinch to diffusion ratio

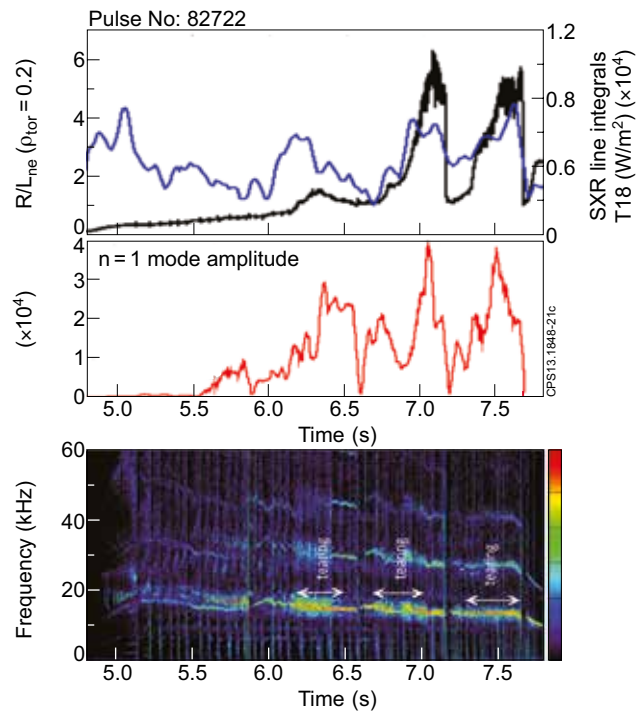


Figure 21: MHD spectrogram (c) and $n=1$ mode amplitude (b) for Pulse No: 82722, compared with central SXR emission (black) and central R/L_{ne} (blue) (a).

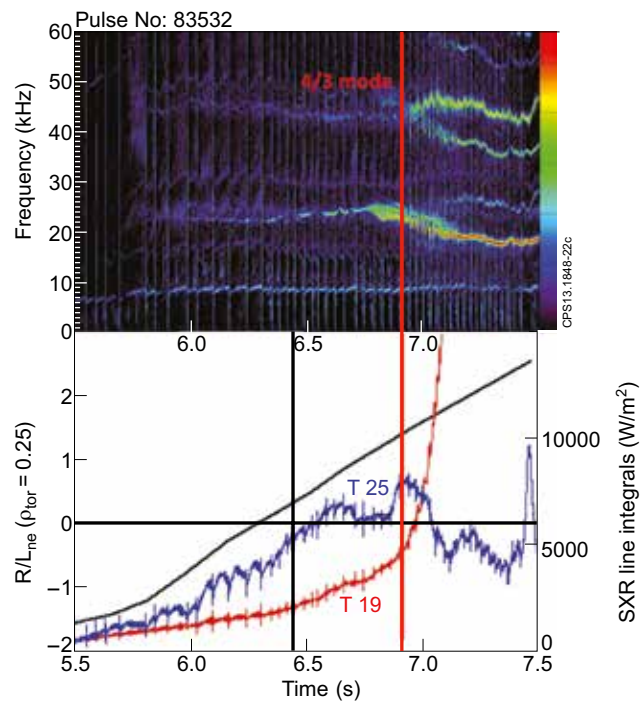


Figure 22: MHD spectrogram for Pulse No: 83532, indicating the onset of a large $4/3$ NTM, correlated with the further increase of the central SXR emission (red), after the first change of rate correlated with the transition of the n_e profiles from hollow to peaked ($R/L_{ne} > 0$, black line). T25 is the off-axis LFS SXR emission.

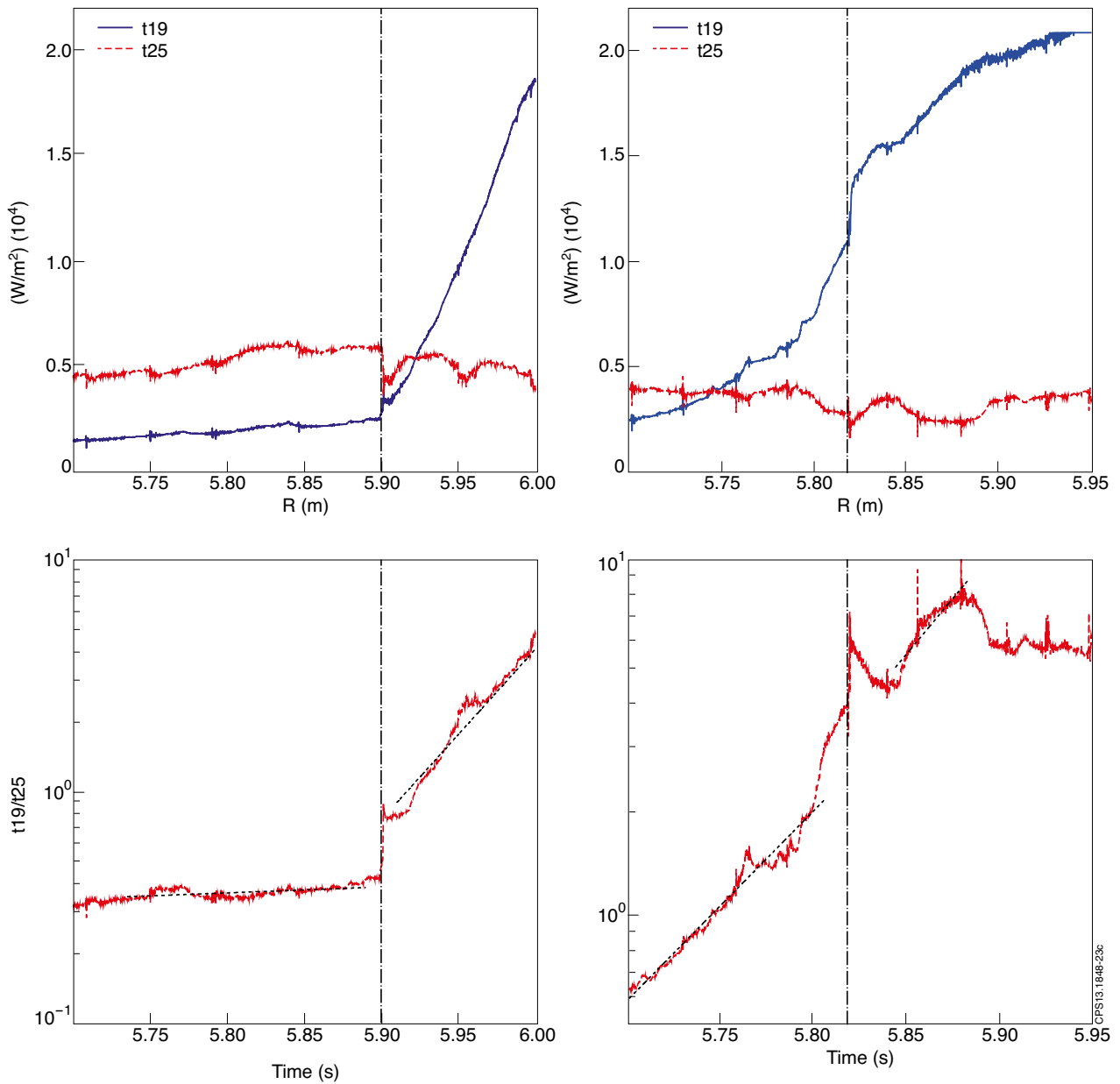


Figure 23: Time evolution of the signals of the LOS t_{19} and t_{25} (a and c) and of their ratio (b and d) of two discharges, Pulse No: 83422 where a 3/2 NTM appears when t_{19} is well below t_{25} (a and b) and Pulse No: 83520 where a 3/2 NTM appears when t_{19} is above t_{25} (c and d). Dashed lines in plots (b) and (d) show the fits of the slopes from which the average peaking rate of W before and after the appearance of the NTM is estimated. The vertical dash-dotted lines mark the time of the onset of the 3/2 NTM.

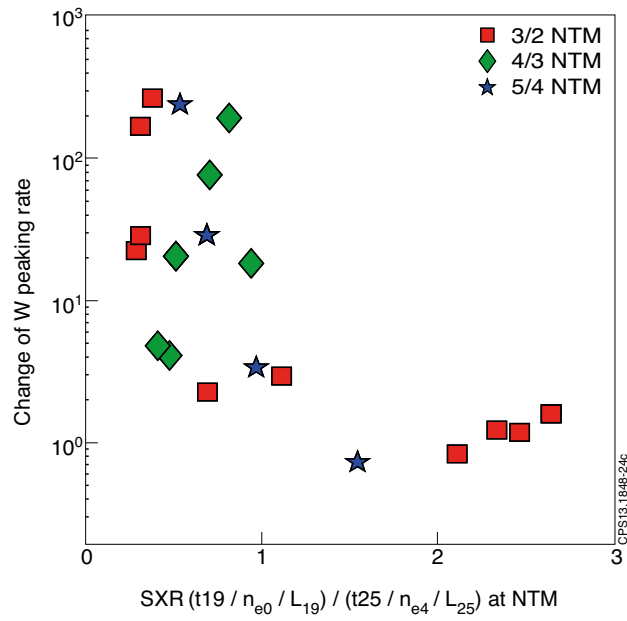


Figure 24: Ratio between the W peaking rate after and before the appearance of a NTM vs a proxy of the W LFS density peaking.